

---

# Outflow of the Antarctic ice sheet:

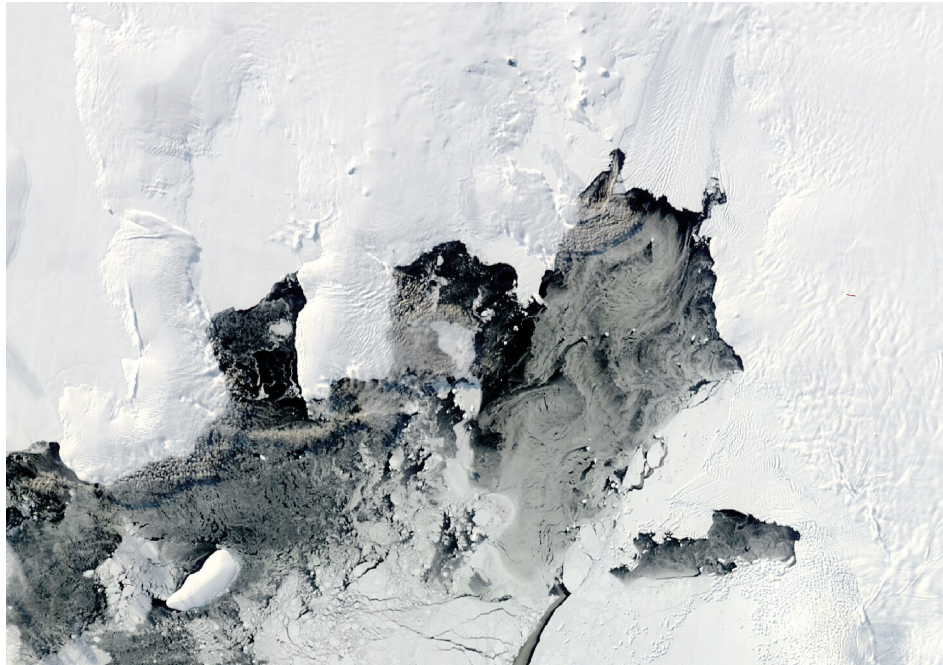
*Is it consistent across models for similar geometries?*

## M2 SOAC Internship Report

---

Marine Le Bescond De Coatpont

Supervisors: Gaël Durand and Cyrille Mosbeux



@NASA: Signs of the season in Pine Island Bay

**University:** Sorbonne Université

**Master:** Ocean, Atmosphere and Climate Sciences

**Student ID:** 28706514

*March 17<sup>th</sup> – August 1<sup>st</sup>, 2025*

# Abstract

The alarming acceleration of global sea level rise rate state the importance of resolving the future climate prediction uncertainties. The Antarctic Ice Sheet is one of the main potential contributing factor to future sea level rise, which contribution is still the most uncertain. To account its impact we look at the ice outflow of the AIS in a key region: the Amundsen Sea Sector.

To do so, we test Schoof 2007 two dimensional equation defining ice flux at the grounding line (line that separates the part of the ice sheet that is resting on the bedrock and the floating part) as a function of the sliding law, the ice rheology, and the ice thickness. Assuming that those parameters are the same across three dimensional ISMP6 model ensemble, we compare the ice flux at the grounding line.

Therefore, we find similar grounding line geometries, using RMSE, based on defined target: the observed grounding line, a moderately retreated grounding line, and a largely retreated one (both model based). We find that, for three dimensional models, the mean ice flux at the grounding line increase with its retreat. Data assimilation models compute ice flux at the grounding line with a better accuracy than Spin up models for the current grounding line geometry. However, for all the chosen targets the large ice flux spread shows the difficulty with which models compute ice flux at the grounding line, even for models with the same sliding law and sliding coefficient. Leading us to discuss the choice of comparison metric and target, and looking if other regions exhibit the same results.

# Acknowledgment

En déposant mes valises dans une ville froide et pluvieuse, je ne m'attendais pas à dire que j'aimerais y rester plus longtemps. Mais ce ressenti n'aurait pas été possible sans l'aide, le soutien, et la présence de nombreuses personnes.

Tout d'abord, un grand merci à mes maîtres de stage Gaël Durand et Cyrille Mosbeux pour leur présence infaillible et le temps qu'ils ont consacré à m'expliquer les détails des modèles ou de la dynamique des glaces / calottes polaires. Merci de m'avoir aidée pour la rédaction de mon rapport et pour l'opportunité de présenter mes résultats à la conférence ISClim de Saclay. Merci de m'avoir soutenue et encouragée pendant mon stage.

Bien évidemment, je remercie l'accueil qui m'a été fait à l'IGE, ainsi que le service administratif et informatique, qui ont été très réactifs et d'une aide précieuse.

Je tiens aussi à remercier le programme OpenReproLab, dirigé par Aurélie Albert et Mykael Vigo, de nous avoir mis à disposition de nombreuses ressources et d'avoir fondé les piliers d'une recherche plus reproductible avec nous. Avec un merci spécial à Mykael pour les heures qu'il a passées à m'aider avec mes problèmes informatiques (et pour les solutions qu'il a trouvées).

Je souhaite aussi remercier tous les membres de l'équipe des Plateformistes, et plus généralement de l'équipe CryoDyn, pour m'avoir donné de nombreux conseils pertinents et pour avoir écouté ma soutenance de stage.

Bien évidemment, je souhaite remercier tous les autres stagiaires de l'IGE pour avoir été gentils avec moi et avoir accepté d'écouter toutes mes présentations, mais surtout de m'avoir donné plein de conseils. Alors merci à Justin pour avoir été un super voisin de bureau et pour m'avoir encouragée dans les moments difficiles, merci à Louise pour sa bonne humeur, son rire contagieux et ses conseils implacables, merci à Achille pour les superbes discussions et les blagues de qualité, merci à Jules pour m'avoir accompagnée à la piscine pour y faire du sport (et surtout parler), merci à Tino pour ses réflexions intelligentes et abouties sur mon travail et son humour, merci à Rémy pour sa bonne humeur, même s'il clique partout et trop vite avec sa souris. J'aurais aussi bien remercié Altaïr, mais il m'a volé la balle !

De plus, je souhaite remercier particulièrement Astrid, Béatrice, Billy & Joe pour leur soutien infaillible, surtout dans les mauvais moments quand ils ont choisi de créer de nouvelles feuilles.

Pour finir, je voudrais remercier toutes les personnes de mon entourage qui ont été là pour moi : merci à mon papa pour les messages d'attention, merci à mon papy et ma mamie de m'avoir remonté le moral et d'avoir écouté longuement mes aventures à Grenoble, merci à tous·tes mes ami·es de Paris qui ont su répondre présents par message ou en face à face, et merci à Caly d'avoir été la chatte adorable qu'elle sait être.

Merci à toutes et à tous !

# Contents

<b>Abstract</b>	i
<b>Acknowledgment</b>	ii
<b>1 Introduction</b>	1
<b>2 The Antarctic ice sheet: a sleeping giant</b>	3
2.1 Mass balance of an ice sheet and its observation. . . . .	4
2.1.1 Mass balance of ice sheet . . . . .	4
2.1.2 Observation of mass balance . . . . .	4
2.2 Ice sheet modeling . . . . .	5
2.2.1 Navier-Stokes equations . . . . .	5
2.2.2 Boundary conditions . . . . .	6
2.2.3 Approximations . . . . .	6
2.2.4 Model initialization . . . . .	7
2.3 Marine Ice Sheet Instability . . . . .	7
<b>3 Hypothesis and Methods</b>	9
3.1 Data . . . . .	9
3.2 Process . . . . .	11
3.2.1 Regions of interest . . . . .	11
3.2.2 Finding similar grounding line geometry . . . . .	12
3.2.3 Grounded mask . . . . .	14
3.2.4 Ice flux at the grounding line . . . . .	16
3.2.5 Choice of the targets . . . . .	17
<b>4 Results and Discussion</b>	18
4.1 Comparison with targets . . . . .	18
4.1.1 Comparison with observations . . . . .	18
4.1.2 Comparison with LSCE GRISLI2 . . . . .	20
4.1.3 Comparison with UNN Ua . . . . .	22
4.2 Discussion . . . . .	25
<b>5 Conclusion and Perspective</b>	28
<b>Appendix</b>	30
<b>References</b>	37

# 1 Introduction

Over the past 500 million years, Earth's climate has experienced substantial fluctuations, with periods significantly warmer than today's climate [Judd et al. [2024]]. While temperature variations are not unprecedented in Earth's history, the current rate of warming is *unprecedented* in its speed and magnitude. It is now unequivocally established that this current global warming is primarily driven by human activities [IPCC [2019]]. Global warming is particularly concerning, not only because of the increase in temperature itself but because of its several consequences on the Earth system. Among these, the ongoing rise in global sea level has become one of the most visible and threatening impacts. Although sea level changes are part of the natural variability of the Earth's system, in the Miocene epoch sea levels were up to 50 meters higher than today [Hansen et al. [2013]], it is the sudden acceleration of the rate of sea level rise between 1971 and today that is unprecedented and human-driven [IPCC [2019]]. The consequences of this acceleration are alarming, by 2040, IPCC predicts that an additional 19.62 million people will be exposed to SLR, increasing the total number of people at risk to 87.73 million people. The frequency of extreme events due to SLR (events currently occurring once every 100 years) will affect one billion people by 2040. Extremes that will increase in frequency in the next 20 years. SLR leading to coastal erosion threatens ecosystems and natural habitats, contributing to the loss of biodiversity. It also leads to the loss of valuable agricultural land, reducing food production, and lowering land values [Hallegatte [2012]]. In addition, economic systems will be affected by frequent floods (as a consequence of SLR and climate change [Calvin et al. [2023]]) requiring extensive infrastructure adaptation, and rehabilitation efforts. These events often cause injury, loss of life, and forced migration, placing additional strain on affected communities [Hallegatte [2012]]. Addressing sea level rise requires long-term planning, approximately over 30 to 50 years, to implement infrastructures to adjust to sea level rise [Calvin et al. [2023]].

SLR is affected by climate change, and it is now possible to observe a drastic increase, going from 0.20 m between 1901 and 2018, with an average rate of  $1.3\text{mm.yr}^{-1}$  from 1901 to 1971, then increased to  $1.9\text{mm.yr}^{-1}$  from 1971 and 2006, and further to  $3.7\text{mm.yr}^{-1}$  from 2006 and 2018 [Calvin et al. [2023]]. The IPCC latest report predicts a global mean sea level rise of  $\sim 0.19$  m under SSP1-1.9 scenario and  $\sim 0.24$  m for SSP5-8.5 scenario by 2050, and  $\sim 0.41$  m for SSP1-1.9 scenario and  $\sim 0.82$  m for SSP5-8.5 scenario by 2100.

There are several factors contributing to global SLR; two of the current main contributors to SLR are the thermal expansion of seawater and the melting of glaciers and polar ice sheets [IPCC [2019]].

The thermal expansion of seawater results from the increase in ocean temperature due to global warming. As seawater warms, its density decreases, causing the water to expand and raise the sea surface height (SSH). This process is directly related to anthropogenic climate change, its contribution to SLR increased from  $0.36\text{ mm.yr}^{-1}$  between 1901 and 1990 to  $1.39\text{ mm.yr}^{-1}$  between 2006 and 2018 [IPCC [2019]].

The second major factor contributing to SLR is the melting of glaciers and polar ice sheets. These freshwater reservoirs are sensitive to warming, which affects their mass balance through the retreat of the equilibrium line (line beyond which the glacier enters the ablation zone), less accumulation, and accelerated ice flow. The combined contribution of continental glaciers and polar ice sheets rose from  $0.91\text{ mm.yr}^{-1}$  between 1901 and 1990 to  $1.62\text{ mm.yr}^{-1}$  between 2006 and 2018 [IPCC [2019]]. Focusing only on the contribution of ice sheets, the 2050 global mean sea level projection for SSP5-8.5 shows an increase of 0.3 m, while by 2100, for the same scenario, the projection points to an increase of 0.9 m. Those projections are from the Ice Sheet Intercomparison Project (ISMIP6), but are still subject to significant uncertainties that require further investigation.

One of them is the contribution of the Antarctic ice sheet (AIS), which had negligible net contribution

during the early 20th century. The AIS contributed  $0.32\text{mm.yr}^{-1}$  to global SLR between 2006 and 2018, IPCC predictions define AIS contribution to SLR as *low confidence*, leaving its real impact uncertain. Indeed, AIS contribution can double depending on the parameterization of the models taken into account [Calvin et al. [2023]]. AIS is the largest ice sheet on the planet, covering 15 million square kilometers under approximately 2300 meters of ice on average, setting its potential in SLR around 58 meters [Calvin et al. [2023]]. This is why AIS plays a key role in predicting the magnitude of future SLR.

Therefore, understanding the dynamics of the polar ice sheet dynamics and developing reliable methods to simulate these dynamics in numerical models is essential to represent their effects in global climate models.

## 2 The Antarctic ice sheet: a sleeping giant

Ice sheets are continental-scale masses of ice that rest on land [NASA [2025]], they form a dome of ice slowly flowing along the topography towards the ocean (for AIS and Greenland ice sheet). Close to the ocean, the ice converges in fjords and valleys where it tends to accelerate, forming ice streams. Those streams discharge the ice into the ocean, creating floating ice shelves, which are still attached to the ice sheet. Indeed, the observations of the ice velocity over Antarctica show that the ice flow at the center of the ice sheet is very slow (i.e. a few meters per year) and increases the closer it gets to the sea (a few hundreds to a few thousands of meters per year in some areas; see Fig. 1, p. 3).

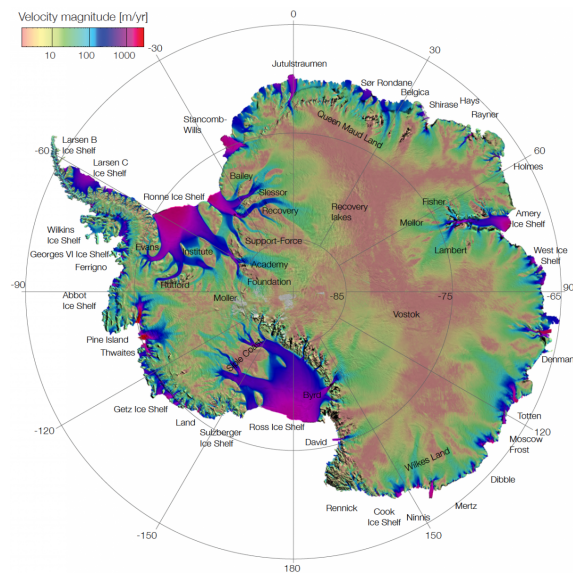


Figure 1: Satellite-based observation of Antarctica ice velocity, in  $\text{m.yr}^{-1}$  from <https://nsidc.org/data/nsidc-0484/versions/2>

Distinctively, the ice sheet is resting on the continental bedrock where the ice shelves are floating in the sea because the upward buoyant force is superior to the ice shelf weight. The limit between the continental ice sheet and the oceanic ice sheet is called the *grounding line* (GL). Past this line, the ice contributes to global SLR. At the ice shelf front, icebergs detach from the ice shelf by fracturing; forming the so-called *calving ice front* (see Fig. 2, p. 4).

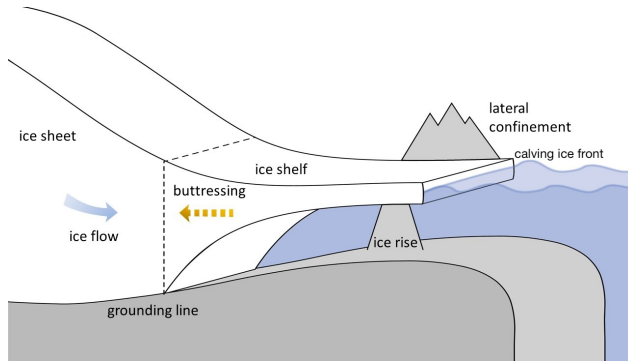


Figure 2: Schematic diagram of ice sheet and ice shelf structures and dynamic, modified image from <https://blogs.egu.eu/divisions/cr/2019/05/10/image-of-the-week-kicking-the-ices-buttressing/>

## 2.1 Mass balance of an ice sheet and its observation.

### 2.1.1 Mass balance of ice sheet

The geometry of the bedrock, as well as the friction at the interface between the ice and the bedrock, largely control ice dynamics. For example, narrow glacier embayments tend to strongly constrain ice flow due to increased lateral friction, whereas in wider or open bays, this friction exerts a weaker control on the ice flow (see Fig.19, p.30).

Ice sheets are formed by densification of snowfalls that transform into ice in the accumulation zone. Ice flows like a viscous fluid under the effect of its own weight. Mass is then lost, through surface melting (primarily in Greenland), basal melting beneath ice shelves, and ice tongues, or calving at the ice front. A simplified mass balance can be erected as the difference between mass gain and mass loss:

$$\Delta B = A - r_a \quad (1)$$

Where  $\Delta B$  is the mass balance budget,  $A$  the accumulation and  $r_a$  the ablation rate.

The ice flow speed is also influenced by various factors, among which the geometry of the glacier embayment and the presence of an ice shelf are particularly important. Indeed, ice shelves play a fundamental role in regulating ice flow velocities. They exert a buttressing effect, providing back-stress opposed to the ice flow towards the sea and thereby reducing ice velocities (see Fig. 2, p. 2 for ice flow and buttressing effect).

### 2.1.2 Observation of mass balance

There are several ways to estimate mass balance using observations. While in situ mass balance observations are often logistically challenging and spatially limited, using remote sensing methods allows to overcome these constraints. These methods have enabled the observation of various key processes involved in ice sheet evolution.

One of the earliest technique is satellite radar interferometry observations, which measures surface displacement by detecting phase differences between radar signals acquired at different times. Using this technique, [Rignot [1998]] estimated a retreat of approximately  $1.2 \text{ km.yr}^{-1}$  between 1992 and 1996 of the Pine Island Glacier grounding line, along with observations of ice thinning.

Later, the detection of mass loss from Earth's ice sheet became possible using the first observation of GRACE (Gravimetry Recovering and Climate Experiment) with gravimetry technique [Velicogna [2009]]. Satellite gravimetry detects the changes in Earth's gravity field that reflect the changes in mass distribution. Corrections are made using glacial isostatic adjustments to isolate the ice mass component.

Another approach is satellite altimetry, which enables estimates of ice sheet mass change by measuring changes in surface elevation. These measurements are then converted in mass changes using ice density models assuming the vertical variability of it. Using this method, combined to other common methods, Cazenave [2006] quantify the mass loss of the ice sheet (Greenland and Antarctica) to estimate their contribution to global SLR.

In addition to elevation and mass change, remote sensing imagery has made possible to estimate the impact of ice shelf collapse. One of the main examples illustrating their impact on the velocity of emissary glaciers is the Larsen B collapse in the Antarctic Peninsula [Scambos et al. [2004]]. After a series of events leading to the collapse of the B section of the Larsen ice shelf, observations of the ice velocities of its emissary glaciers showed an acceleration of the ice flow the following year. On the contrary, emissary glaciers with remaining ice shelves attached did not show any substantial change in velocity (see details in Fig.20, p.31). This highlights the critical role of ice shelves in the dynamics of emissary glaciers and, by extension, Antarctic mass balance (AMB).

More recently, the IMBIE team [The IMBIE Team [2020]], provided a comprehensive estimate of the Greenland Ice Sheet mass balance from 1992 to 2018 using 26 satellite datasets. It combines altimetry, gravimetry, and the input–output method (estimate the surface mass balance from climate models and combine it with observation of ice velocity and thickness to calculate ice discharge to the ocean), alongside climate models, to distinguish mass losses due to surface processes (e.g., meltwater runoff) and glacier dynamics. This reconciliation highlights that Greenland lost around 3,902 Gt of ice over the period, contributing 10.8 mm to global SLR. The synthesis made by IMBIE is important for demonstrating the consistency across observation methods and underlining the dominant role of atmospheric warming in ice loss variability. Although these methods provide consistent results, their associated uncertainties can, in specific regions (East Antarctica), be on the same order of magnitude as the estimated mass balance itself.

## 2.2 Ice sheet modeling

*The primary objective of a glacier or ice flow model is to simulate its evolution over time and space.*

An ice sheet model incorporates climate inputs, such as atmospheric conditions (e.g., precipitation, surface melt, surface temperature) and oceanic conditions (using temperature and salinity to parameterize a basal melt rate or directly using melt rate from the ocean model) from climate models. These inputs are used to drive changes from an initial ice sheet configuration (Section 2.2.4). Once initialized, the model solves the physical equations governing the ice dynamics, taking into account boundary and initial conditions, such as basal friction.

### 2.2.1 Navier-Stokes equations

In theory, a Newtonian fluid responds to the Navier-Stokes equations, which rely on the principle of mass and momentum conservation. Because ice can be considered incompressible and viscous effects are dominant, ice flow can be resolved with a Stokes flow approximation:

$$\operatorname{div} \mathbf{v} = 0 \quad (2a)$$

$$\operatorname{div} \boldsymbol{\tau} = \rho_i g \quad (2b)$$

with  $\mathbf{v}$  the velocity field,  $\rho_i$  the density of the ice,  $g$  the gravity acceleration, and  $\boldsymbol{\tau}$  the Cauchy stress tensor defined as:

$$\boldsymbol{\tau} = \boldsymbol{\tau}^D + p\mathbf{I} \quad (3)$$

where  $p = -\frac{1}{3}\text{tr}(\boldsymbol{\tau})$ ,  $\mathbf{I}$  is the identity tensor, and  $\boldsymbol{\tau}^D$  is the deviatoric tensor. The deviatoric stresses are linked to strain rates (i.e., velocity gradients) through a constitutive law called the Glen's flow law [Glen [1955]] (it shows the dependence of ice viscosity to strain rates):

$$\boldsymbol{\tau} = 2\eta\dot{\boldsymbol{\epsilon}} \quad (4)$$

where  $\boldsymbol{\tau}$  is the deviatoric stress,  $\dot{\boldsymbol{\epsilon}}$  is the strain rate of the ice, and  $\eta$  is the viscosity of the ice:

$$\eta = \frac{1}{2}(EA)^{-\frac{1}{n}} I^{\frac{(1-n)}{n}} \quad (5)$$

with  $E$  an amplification factor,  $I$  a part of the ice strain rate, and  $A$  the temperature-dependent ice fluidity, defined as:

$$A = A_0 e^{-\frac{Q}{RT}} \quad (6)$$

with  $A_0$  the reference fluidity,  $Q$  the energy of activation,  $R$  the gas constant,  $T$  the temperature, and  $n$  Glen's exponent, typically  $n = 3$ , which induces a non-linearity in the system, and therefore increases the complexity of the system to solve.

### 2.2.2 Boundary conditions

Additionally, at the upper surface and at the ice base of floating shelves, a traction-free boundary condition is applied. In grounded areas, a basal friction is applied by applying a sliding or friction law such as:

$$\boldsymbol{\tau}_b = -\beta^{m-1} \mathbf{v}_b \quad (7)$$

where  $m$  is the coefficient of the sliding law, and  $\beta$  is the basal parameter including the effective pressure, the presence of water which lubricates the ice-base interface, and the bedrock properties such as its roughness.

The sliding law is one of the most important equation for ice sheet models. The early formulation of this law was by [Weertman [1957]] who described glacier sliding over a rough bed through a power-law relationship between sliding velocity and basal shear stress. To take into account more complex conditions, [Schoof [2005]] proposed a law allowing the transition between Weertman "sliding type" and Coulomb behavior. making it more suitable for numerical implementation and partially dependent on effective pressure. [Tsai et al. [2015]] developed a hybrid formulation between Coulomb and Weertman regimes based on effective pressure. Finally, [Brondex et al. [2017]] demonstrated that the GL dynamics are highly sensitive to the chosen friction law, emphasizing the importance of accurately representing bed type and basal processes in ice flow models.

### 2.2.3 Approximations

Resolving those equations (Eq. 2) at the continental scale is still very costly. Even though these models represent the complexity of the ice flow, they are computationally expensive and often impractical for long-term or large-scale simulations. This is why approximations of the Stokes equations have been developed, enabling models to represent key processes at a lower cost. Two of the main approximations for ice sheet models are the *shallow ice approximation* (SIA) and *shallow shelf approximation* (SSA).

The SIA is suitable for grounded ice where vertical shear dominates (i.e., where the basal friction is high and ice flows slowly). In practice, SIA is generally applied to the grounded interior regions of the ice sheet and to glaciers whose thickness is small relative to their horizontal extent. By neglecting most stresses of the

Stokes equation, this approximation is fast to resolve but does not deliver great results in high-velocity areas. On the opposite, the SSA can be applied in regions where longitudinal stresses dominate over vertical shear stresses (i.e., where the basal friction is low and ice flows fast). Horizontal velocities are therefore considered constant over the ice column. Therefore, the approximation is used in ice streams and in floating ice shelves where extensional flow is largely dominant, neglecting stress components which are negligible in principal.

Additionally, some hybrid models use both approximations to better describe ice flow. However, the transition between SIA and SSA within those models introduce a source of uncertainty, as the switch between regimes can be difficult to treat numerically.

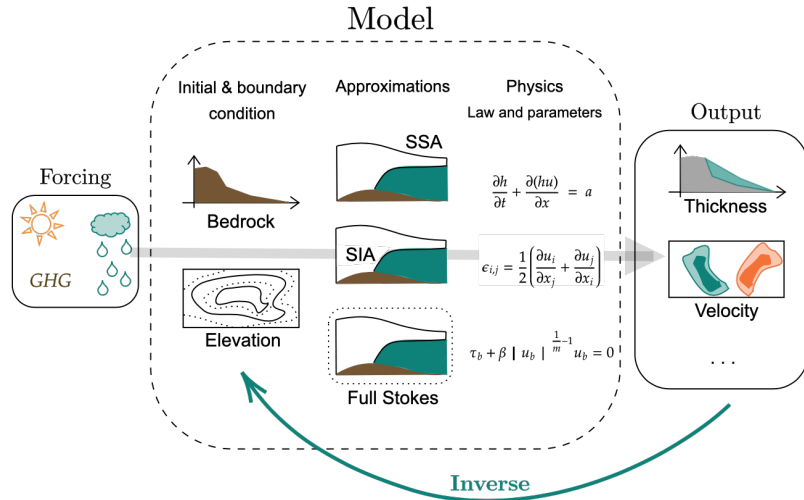


Figure 3: Schematic diagram of the structure of an ice sheet model. From left to right, forcing box represents the climate and anthropic (e.g., Greenhouse gases (GHG)) forcing, the model box illustrates the internal functioning of an ice sheet model (equation illustrated are from top to bottom: the mass conservation, infinitesimal strain tensor and, Weertman's law) and, the output box shows potential model output.

#### 2.2.4 Model initialization

Two types of model initialization are employed: *spin-up* and *inverse* models.

In the spin-up approach, the model is forced with past climate conditions (e.g., temperature, geothermal flux, and surface mass balance) and is run forward from the past to the present, and then into the future. This allows for the long-term adjustment of the model to external forcing. However, the present-day geometry may deviate from observations, and the models typically operate at coarse spatial resolution (because of the time it has to run). Represented with the gray arrow in Fig. 3, p.7.

In the other approach, the inverse model uses the observed geometry to create the initial conditions and calibrate parameters, such as basal friction, to fit the observed geometry and/or observed surface velocities. After the initial step, models typically follow one of the two approaches, either they are run over a relaxation period with constant climate forcing to allow internal fields (e.g., velocity, thickness) to adjust and stabilize around the observed geometry, or they use inverse methods that directly optimize basal parameters to match the observed geometry. In Fig. 3, p.7 inverse models are represented with the teal arrow.

## 2.3 Marine Ice Sheet Instability

In 1974, Weertman [Weertman [1974]] made a first demonstration that the ice flux at the grounding line is an increasing function of the ice thickness at the grounding line. This relationship set the theoretical foundation

for what is now known as the Marine Ice Sheet Instability (MISI) (see Fig. 4(a), p.8).

A marine ice sheet is an ice sheet that rests on bedrock below sea level, and its GL (the point where the ice sheet detaches from the bed and begins to float) plays a crucial role in its stability. The marine ice shelf is subject to basal melting, due to the oceanic heat flux from below. This melting reduces the ice shelf's thickness and the associated buttressing effect, which lowers the longitudinal stress resistance at the grounding line. If the GL is situated on a retrograde bed slope (i.e., a bed that deepens inland), a small retreat of the GL leads it to a deeper part of the bed. At this new position, the ice thickness is greater, which according to Weertman's theory, results in increased ice flux across the grounding line.

This forms a positive feedback loop; greater ice thickness leading to greater flux accelerating the retreat causing an even thicker ice at the new grounding line position, and so on. This instability implies that once retreat is initiated on a retrograde slope, it can become self-sustaining, potentially leading to a rapid and irreversible collapse of the marine ice sheet.

The grounding line can only stabilize if it encounters a prograde slope (i.e., a bed that shallows inland), where the feedback becomes negative: retreat would lead to shallower bed depth leading to thinner ice, and reduced flux, allowing the grounding line to potentially find a new equilibrium. If such stabilization does not occur, the process may continue until the entire marine ice sheet collapses, contributing significantly to global sea-level rise.

However, Weertman paper was disputed for several years (30 years) lacking in practical observation. It was only in 2007 that Schoof in [Schoof [2007a]] using a 2D flow line model demonstrate the existence of MISI and its implication on the retreat of the GL and that its stability depends on the slope of the bedrock. Nonetheless, [Gudmundsson et al. [2012]] demonstrated, using a three-dimensional model, that the presence of buttressing forces can regulate the grounding line retreat and that MISI did not always occurs in the presence of a retrograde slope.

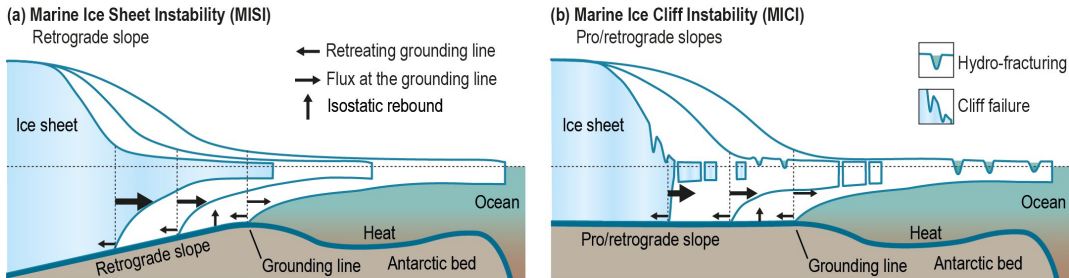


Figure 4: Schematic representation of MISI (a) and MICI (b) from Pattyn [2018]

### 3 Hypothesis and Methods

As discussed in the previous chapters, understanding the dynamics of ice flow in AIS is crucial for improving the reliability of SLR model projections. Among various metrics used to assess the evolution of the ice sheets (e.g., mass change, surface mass balance, basal melt), the ice flux at the grounding line is particularly important. This flux provides insight into how much ice is being transferred from the grounded interior to the floating ice shelves, thereby directly influencing ice loss and its contribution to SLR. Therefore, looking at the ice flux at the grounding line is of major importance to determine the future impact of AIS on SLR and the uncertainty attached to ice sheet models.

In two-dimensional flow line models, [Schoof [2007b]], the ice flux (IF) at the grounding line can be defined as:

$$q(x_g) = \left( \frac{\bar{A}(\rho_i g)^{n+1} \left(1 - \frac{\rho_i}{\rho_w}\right)^n}{4^n \beta} \right)^{\frac{1}{m+1}} [h(x_g)]^{\frac{m+n+3}{m+1}} \quad (8)$$

where  $x_g$  is the position of the grounding line,  $\rho_i$  and  $\rho_w$  are the density of the ice and the water,  $\bar{A}$  is the depth-averaged temperature-dependent fluidity,  $n$  is the given exponent for Glen's law, and  $\beta$  and  $m$  are the sliding coefficient and exponent. The parameters  $A$  and  $n$  characterize the ice rheology, and  $\beta$  and  $m$  define the sliding law of the model. Therefore, if the sliding law and Glen's law are similar across models, and the ice thickness at the GL is similar, then according to Eq. 8 the models should have the same IF at the GL.

While Eq. 8 is derived for a two-dimensional flow line model, the ISMIP6 ensemble is composed of three-dimensional (or plan-view two-dimensional) ice sheet models. This leads to the following question: can Eq. 8 represent accurately the variation of IF at the GL since the ISMIP6 models enable the presence of buttressing from ice shelves and/or narrow valleys with high lateral drag [Gudmundsson et al. [2012]]). To test this theoretical expectation, we use the ISMIP6 model ensemble to assess whether the grounding line ice fluxes of the different models converge when the geometry is comparable across models.

#### 3.1 Data

ISMIP6 constitutes a set of simulations following an experimental protocol part of the projection of CMIP6 (Coupled Model Intercomparison Project), which is described in Nowicki et al. [2020] . It focuses on high emission scenarios (RCP8.5) of IPCC –but also investigates the ice sheet response to low emission scenarios (RCP2.6)– and samples CMIP models based on how well they represent present-day Antarctic climate, to have a large sample of forcings. The models that have been selected for ISMIP6 are described in Table 1.

During the internship, some specific model outputs have been used to do the computation needed. They are defined in Table 2. Those output variables are contained in netCDF files mapping the entire AIS with stereopolar coordinates, with  $x$ ,  $y$  axes that represent the distance from the south pole and a *time* coordinate going from 2016 to 2301 with a yearly climatology.

Table 1: List of ISMIP6 models analyzed during the internship, describing the type of model, initialization of the model geometry as the following: spin-up (SP), data assimilation, inversion, (DA) [Seroussi et al. [2019]], the rheology and the sliding law (the sliding laws are determined by the articles next to the model's name) used in the model

Model	Initialization geometry	Rheology (Glen's law)	Sliding law
DC ISSM [Larour et al. [2012]]	DA	Norton-Holl	Weertman power law
IGE ElmerIce [Hill et al. [2023]]	DA and short relaxation	Glen flow law	Regularized Coulomb
ILTS SICOPOLIS [Sato and Greve [2012]]	Paleo SP	Regularized Glen flow law	Weertman sliding law
LSCE GRISLI [Quiquet et al. [2018]]	SP with target for ice thickness	Norton-Holl conservative law	power-law basal friction (Weertman) and SSA as sliding law
NORCE CISM2 [Robinson et al. [2022]]	DA and SP	Glen flow law	Coulomb friction law
PIK PISM [Hill et al. [2023]]	SP	Nye Paterson	Power law Mohr-Coulomb
UCM Yelmo [Robinson et al. [2022]]	DA	Glen flow law	SSA as sliding law and Coulomb friction law
ULB fFETISh-KoriBU2 [Pattyn [2017]]	DA	Glen's flow law	Weertman sliding law (power law) and Coulomb friction law
UNN Ua [Hill et al. [2023]]	DA and inversion	Glen flow law	Regularized Coulomb
UTAS ElmerIce [Seroussi et al. [2014a]]	DA	Norton-Holl	Weertman sliding law

Table 2: List of variables from ISMIP6 models used in this work, modified version from [Seroussi et al. [2019]]

Variable	Acronym	Unit	Description
Ice thickness	lithk	m	The thickness of the ice sheet
Surface elevation	orog	m	The altitude or surface elevation of the ice sheet
Base elevation	base	m	The altitude of the lower ice surface elevation of the ice sheet
Bedrock elevation	topg	m	The bedrock topography
Basal velocity in y	yvelbase	$m.s^{-1}$	v-velocity at land ice base
Basal velocity in x	xvelbase	$m.s^{-1}$	x-velocity at land base
Mean velocity in y	yvelmean	$m.s^{-1}$	The vertical mean land ice velocity is the average from the bedrock to the surface of the ice
Mean velocity in x	xvelmean	$m.s^{-1}$	The vertical mean land ice velocity is the average from the bedrock to the surface of the ice
Grounding line flux	ligroundf	$kg.m^{-2}.s^{-1}$	Loss of grounded ice mass resulting at grounding line. Only for grid cells in contact with grounding line

All the models have different resolutions and gridding systems but have been regredded to regular rectangular grids, as requested in the ISMIP6 protocol. However, due to the different model resolutions, some models have been gridded at a 4 km x 4 km resolution, while others have been gridded at a 8 km x 8 km or 16 km x 16 km. For this work, we have regredded all the models at the highest resolution (4 km x 4 km), using a linear interpolation scheme, to facilitate the calculation and comparison of those different models, without losing any information .

## 3.2 Process

To compute the IF at the GL for a similar geometry, we first need to compute the part of Antarctica that lies on the continent, defined as the grounded mask, for each model. Then, compare the grounded mask of each model to a chosen target (among all the models), and finally compute the IF at the GL for the different regions of Antarctica.

### 3.2.1 Regions of interest

The Amundsen Sea sector is one of the largest contributors to sea level rise in Antarctica, and where most of the major changes in mass balance are observed. Rapid ice-shelf thinning and grounding line retreat have been observed in the region over the last decades [Rignot et al. [2014]]. Studies have also shown that the region is particularly prone to even faster ice shelf and grounding line retreats [Feldmann and Levermann [2015]]. In addition, [Feldmann and Levermann [2015]] have found that the retreat of Amundsen's grounding line could initiate and amplify the retreat of the Ross grounding line. The rapid ice loss in these two regions could trigger the collapse of the entire East AIS and a 3-m increase in sea level.

Therefore, in this work, the focus will be on Amundsen sea (see Fig. 5, p. 12).

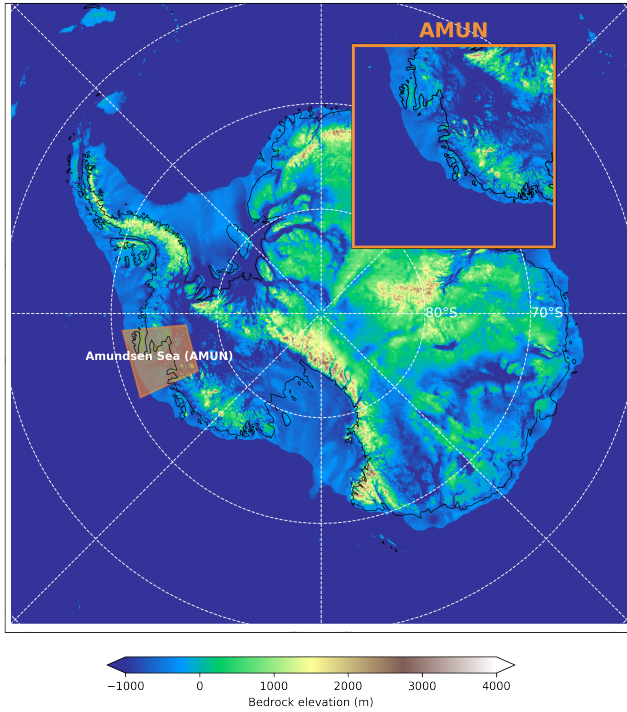


Figure 5: Observation of the bedrock from BedMachine v2, with a focus, on the top, on Amundsen sea (AMUN), and on the bottom on Ross sea (ROSS)

All the following computations have been done on the region and the next steps of the method are applied to this region too. The regional definitions are based on the 8 km NetCDF mask from Zwally, which delineates the main drainage basins of Antarctica (see Fig. 21, p. 31).

### 3.2.2 Finding similar grounding line geometry

The first objective of our method is to find similar geometries across all the experiments and models. For that, we the geometry of the grounding line. We define a target model that serves as a reference against which all other models, referred to as *comparison* models—are evaluated.

**Hausdorff distance** The first line of research was to use the *Hausdorff distance* (HD) to find similar geometries across the models. The HD is a measure of similarities between two sets of points [Ryu and ichiro Kamata [2021]]. It computes the maximum distance between two points in a geometrical shape; here  $X = \{x_1, x_2, \dots, x_n\}$  and  $Y = \{y_1, y_2, \dots, y_n\}$  are two sets of points (represented in Fig. 6, p. 13).

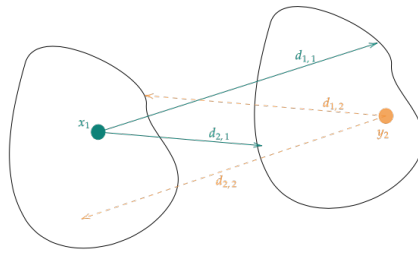


Figure 6: Schematic diagram of the computation of Hausdorff Distance

The HD is defined as:

$$H(X, Y) = \max(h(X, Y), h(Y, X))$$

Where  $h(X, Y)$  is the directed HD from  $X$  to  $Y$ , it represents the maximum distance between each point of  $x \in X$  and the  $y \in Y$ . The directed HD are not symmetric one to another. When in theory the HD seems to be a great metric to find similarities between GL geometry, in practice the usage of the HD does not find a precise match between the target and the comparison mask. This is due to the asymmetry of the HD, which takes into account the maximum of the directed HD. Therefore it switches from one directed distance to another without consistency (see Fig. 22, p. 32 for an example).

Given the poor results of the HD, we used a different metric to find a similar GL geometry.

**Root Mean Square Error (RMSE)** The RMSE is a measure that computes the quadratic mean of the difference between the observed and sample data, here the target and the comparison mask. The RMSE is defined as:

$$RMSE = \sqrt{\frac{1}{n} \sum_{i=0}^n (x_i - y_i)^2}$$

Where  $x_i$  and  $y_i$  are the points in the sets of points previously defined. In this work, we use the RMSE from *xskillscore* python library, that is a function specifically made for *xarray* datasets.

To evaluate the method, we use a simple case study; a circle with a growing radius over time and a target that is on the growing circle. This allows us to see if a clear minimum can be defined and if the method is efficient. For the theoretical study, the RMSE defines a clear minimum distance of zero between the target and the comparison targets, and has an expected behavior with a decrease of the RMSE before meeting the target and an increase after meeting the target (e.g. Fig. 7, p. 14)

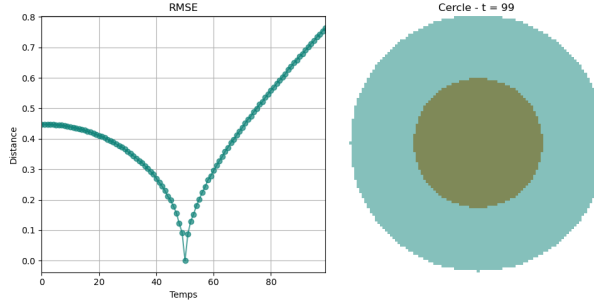


Figure 7: Study case of the RMSE, on the left the evolution of the RMSE over the time, and on the right a frame of the target circle and the comparison circle

We can test it on a target and comparison masks to see if, in the case of grounded geometries, the RMSE exhibit a clear minimum. We take a target from one experiment of a model and compare it to the different experiments of this same model. This should show a precise minimum of RMSE when the chosen experiment is compared to itself. The results show that a clear minimum is observed and that the behavior of the RMSE over time is expected for the comparison within one model (see Fig. 23, p. 32). The same behavior is observed when comparing a target from one model and the experiment of another model (see Fig. 8, p. 14).

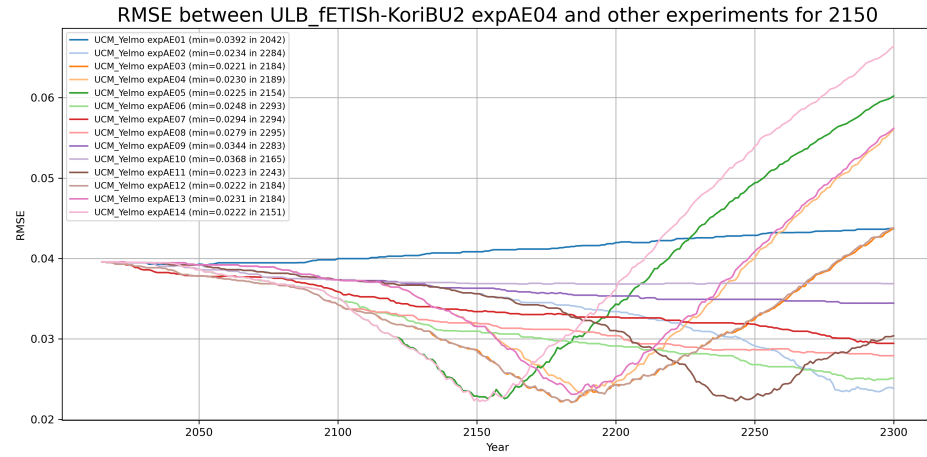


Figure 8: Example of the RMSE over time, where ULB\_fETISH-KoriBU2 expAE04 2150 is the target and compared to UCM\_Yelmo experiments with the year of the best match and corresponding minimum RMSE

To identify the optimal comparison points, we first determine the year corresponding to the minimum RMSE for each experiment of a model and store these values in a CSV file. Then, for each model, we extract the experiment and year with the lowest RMSE for each model and save the result in a second CSV file. The subsequent comparisons are based on this model-specific minimum RMSE information.

Therefore, to find those similar geometries, we need to compute the grounded mask for all the models.

### 3.2.3 Grounded mask

To do the comparison between the grounding line of the models, we introduce the *grounded mask*. The grounded mask is defined as the mask that determines the part of the ice sheet that is grounded (behind the GL). It is therefore directly related to the grounding line. We chose this metric because if models have the same GL, they have the same ice thickness at the GL (assuming the bedrock is the same along models).

To compute this grounded mask we used the bedrock elevation (*topg*) and the ice base/lower surface of the ice sheet (*base*) variables. If the ice sheet lies on the continental bedrock, the difference between those two variables is zero, and if we are in an ice shelf configuration, then the difference is negative (see Fig. 9, p. 15).

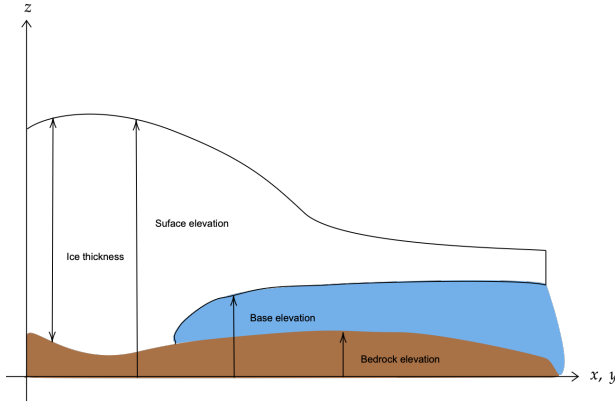


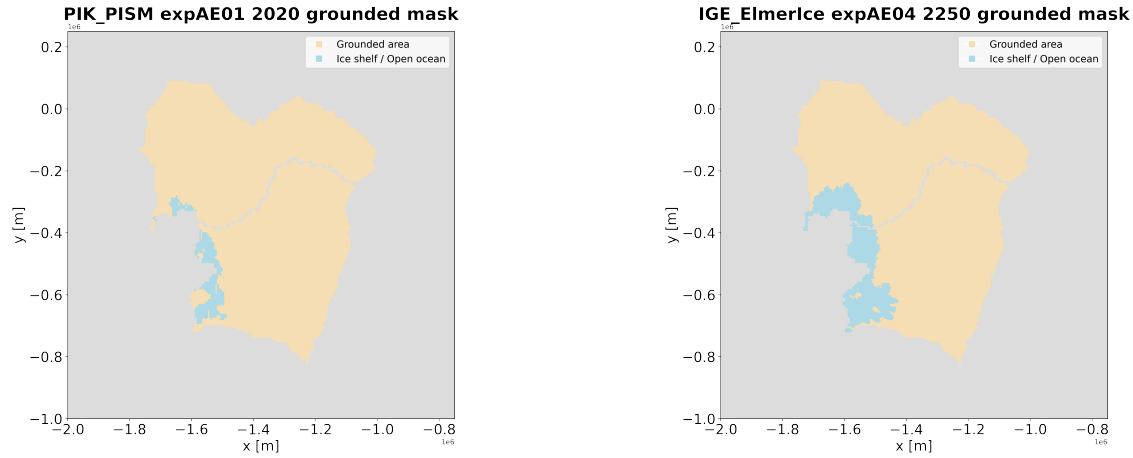
Figure 9: Schematic diagram of the ice thickness, surface elevation, base elevation, and bedrock elevation variables output for the ice sheet.

Accordingly, the grounded mask is computed using this formula:

$$topg - base = \begin{cases} = 0 \pm \epsilon & \text{ice is grounded} \\ < 0 & \text{ice is floating} \end{cases} \quad (9)$$

Where  $\epsilon$  is a threshold value arbitrarily set to  $\epsilon = 0.01$  m to compensate for numerical errors and uncertainties in the outputs of the models.

The resulting grounded masks are shown below, where the brown represents the grounded part of the ice sheet, and the blue represents the floating part.



(a) PIK PISM grounded mask for exp 1 on 2250

(b) ElmerIce grounded mask for exp 4 on 2250

Figure 10: Grounded masks in AMUN region, where yellow is the grounded part of the ice sheet, blue the floating part

### 3.2.4 Ice flux at the grounding line

Once the similar geometries are found, we can compute the ice flux at the GL and see if the ice fluxes are also similar.

**Computation of the ice flux at the grounding line** Because the *lgroundf* is not a required output for the ISMIP6 models, only a few models have this output. In addition, some of the models had unit issues (notably ULB\_fETISH-KoriBU2) which made the IF comparison laborious.

Therefore, we will compute the IF at the GL using an already existing code written by Cyrille Mosbeux and modified to fit the work done in this report.

To compute the IF at the GL the python script finds the grounding line coordinate using the same methods as for the grounded mask, then uses the *lithck*, *xvelmean*, and *yvelmean* to calculate the IF at the coordinate of the GL. The IF is calculated at each point of the grounding line:

$$q(x_g) = H \times v \times dl \quad (10)$$

where  $q$  is the IF in  $m^3.yr$ ,  $x_g$  is the position of the GL,  $H$  is the ice thickness at the GL in  $m$ ,  $v$  is the norm of the mean velocity (in  $m.yr^{-1}$ ) in the direction normal to the segment  $dl$  of the grounding line, with one extremity located in  $x_g$ .

**Ice flux at the grounding line for a region** When the IF at the grounding line is saved in the netCDF file, we can select the region to compute the total IF in this region using:

$$q_{\text{total}}(x_g) = S \times \sum_{i=0}^N q_i(x_g)$$

where  $q_{\text{total}}(x_g)$  is the total IF at the GL in  $Gt.yr^{-1}$ ,  $S$  the surface area of a grid cell in  $m^2$ ,  $N$  the number of cells with a IF at the GL in the region.

**Ice flux comparison** To do an IF comparison, we plot the IF at the GL at the time corresponding to the minimum of RMSE between each model and the target. Since the year of minimum of RMSE differs between each model, the comparison is done at a hypothetical time  $t$  which corresponds to the year of minimum of RMSE for each model. To evaluate the temporal evolution of the IF at the GL, we also plot the IF at  $t - 5$  to  $t + 5$  year, which provide information on the model trend before and after the best match with the target.

### 3.2.5 Choice of the targets

Choosing an appropriate target model is essential to find meaningful comparisons with the other models across Amundsen Sea sector.

First, we compare the models with the GL derived from BedMachine, to assess whether each model reproduces, at some point in time and to some extent, a geometry that is consistent with observations.

Then we chose two targets (based on [Seroussi et al. [2024]]), one with a limited GL retreat (not very retreated from the initial position) and another with a large GL retreat (see Fig. 11, p.17).

The comparison will be done on those selected targets Tab. 3 regardless of the climate forcing and year as long as the grounding line geometry is similar.

Table 3: List of the grounding line (advanced and retreated) target for Amundsen sea sector Seroussi et al. [2024]

Region	Observation	Limited GL retreat	Large GL retreat
Amundsen (AMUN)	BedMachine	LSCE_GRISLI2 exp 4, 2150	UNN_Ua exp 4, 2250

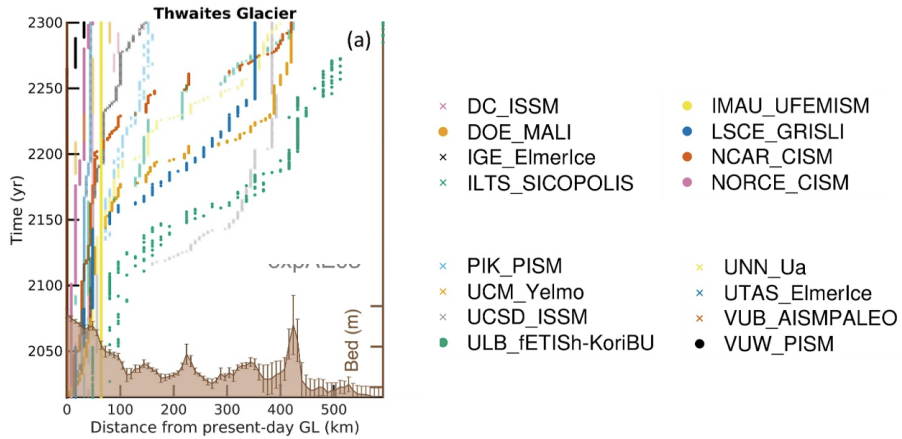


Figure 11: Modified figure from [Seroussi et al. [2024]], representing the relative distance of the grounding line, of every ISMIP6 models, over time for expAE04, on the left the cross-section of *Thwaites Glacier* in the Amundsen embayment and on the right the cross-section of *Siple Coast* in the Ross sea

This research internship benefited from the support of the laboratory's digital platform, as part of the **OpenReproLab** initiative. The students had access to a cloud-based computing environment. They also took part in weekly training sessions focused on coding practices and data management aimed at improving the reproducibility of results. These trainings, along with support throughout the internship from members of the digital platform, introduced tools, methods, and a work organization that promote direct integration of the project into the methodologies and best practices to deliver open and reproducible science.

# 4 Results and Discussion

In this section, we present the results of the geometry comparison between the different models from the ISMIP6 ensemble. Unlike typical ice sheet model intercomparisons (e.g., Seroussi et al. [2024]), which evaluate geometries at specific time steps, we compare geometries independently of time. For example, while two models might differ significantly in their 2025 geometries, the 2025 geometry of one model could closely resemble the 2125 geometry of another.

The metric used for this comparison is the grounding mask, which, as discussed in the previous chapter, represents the extent of the grounded ice sheet. Considering different target geometries, we identify, using RMSE, the model whose grounded mask best matches the target. The other model grounded masks are presented in the Appendix. Once the best-matching geometry is identified for each comparison model (i.e., the time at which we find the lowest RMSE), we compare the IF at the GL for each model at the time of this best match.

Because ice sheet dynamics vary significantly by region, we focus our analysis on a single basin. The Amundsen Sea sector was a natural choice due to its highly dynamic ice flow and the potential for substantial retreat over the ISMIP6 simulation period.

## 4.1 Comparison with targets

### 4.1.1 Comparison with observations

The ability of ice sheet models to accurately represent the current state of the Antarctic Ice Sheet is crucial for producing reliable future projections. Therefore, we begin by comparing the ISMIP6 ensemble to BedMachine, which compiles multiple observational datasets, to provide the best Antarctic ice sheet geometry available. Using the BedMachine grounding mask as the target, we identify the model grounding line masks that best match it, based on the minimum root mean square error (RMSE), as summarized in Tab. 4.

Table 4: Summary of the model experiments and corresponding year with the lowest RMSE compared to BedMachine in the Amundsen region (sorted by increasing RMSE)

Simulation	Experiment	Year	RMSE	Initialization
IGE_ElmelIce	expAE04	2016	0.011235	DA
NORCE_CISM2-MAR364-ERA-t1	expAE04	2054	0.012681	DA and SP
UTAS_ElmelIce	expAE01	2016	0.013182	DA
UNN_Ua	expAE01	2016	0.014774	DA ans inversion
ILTS_SICOPOLIS	expAE02	2035	0.016357	Paleo SP
PIK_PISM	expAE04	2019	0.016436	SP
LSCE_GRISLI2	expAE04	2108	0.017258	SP with geometry target
DC_ISSM	expAE01	2016	0.017457	DA
UCM_Yelmo	expAE05	2235	0.018196	DA
ULB_fETISH-KoriBU2	expAE14	2024	0.024129	DA

The best match is obtained with IGE Elmer/Ice, experiment 4 in 2016, which uses data assimilation (DA) and inverse methods to construct their present-day initial state. Most ISMIP6 models rely on BedMachine

v2 for building their initial geometry, which should lead to a good match between these model geometries and BedMachine. From Table 1, we can confirm this expectation: models using DA have matching years close to the start of the simulation (2015–2017), except for UCM Yelmo, whose best match occurs in 2235. The few years of difference between the BedMachine reference year (i.e. 2015) and the comparison model best matches can be explained by the relaxation phase used by some of these models. This phase consists in letting the model run forwards for a few years (i.e. adapting the surface to the physical constraints and forcings). This phase is often needed to smooth out ice flux divergences resulting from remaining inconsistencies between initialized variables [Seroussi et al. [2014b]]. In contrast, for models using spin-up (SP) techniques, based on historical climate reconstruction, the matching years vary significantly, ranging from 2019 to 2108. Overall, most models are able to reproduce the observed geometry, to some extent. However, small differences at the pixel scale can correspond to discrepancies of several kilometers in the actual GL position, and SP models generally begin with a GL geometry that differs substantially from the observed one.

After identifying the best match for each model, we visually compare these with the target. Fig 12 shows the diagnostics for the target (BedMachine) and the best match (IGE Elmer/Ice) (see Fig. 25, p. 33 for the other matches).

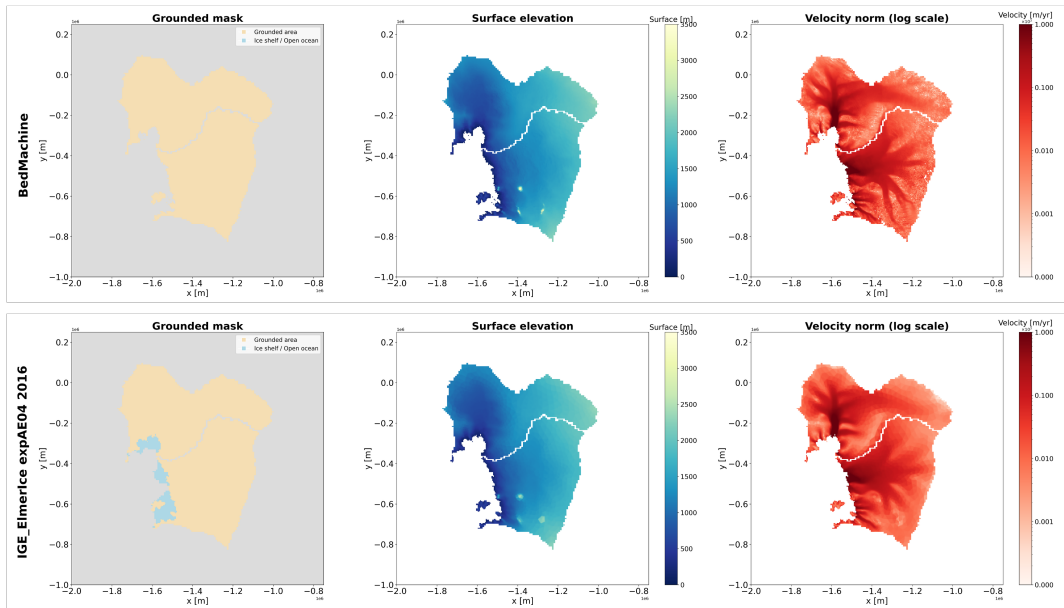


Figure 12: Plot of the diagnostic, for (first line) the target BedMachine, and (second line) for IGE Elmer/Ice experiment 4 in 2016. From left to right: the grounding mask, surface elevation in m, and the velocity in  $\text{m.yr}^{-1}$ .

The figure includes surface elevation (a proxy to ice thickness since for most models, the bedrock geometry follows BedMachine) and velocity fields (norm of the velocity vector), which are essential for computing the ice flux at the grounding line (see Eq. 10). If comparison models exhibit similar velocities and ice thicknesses to the target, their computed flux should be comparable.

The ice fluxes at the grounding line for the target and matched models are shown in Fig. 13. Because the matching years differ across models, we use a relative time axis where  $t$  is the year of minimum RMSE. To evaluate the ice flux change as the ice geometry evolves over a close time around the matching year, we also compute the IF values and plot them from  $t - 5$  to  $t + 5$  years.

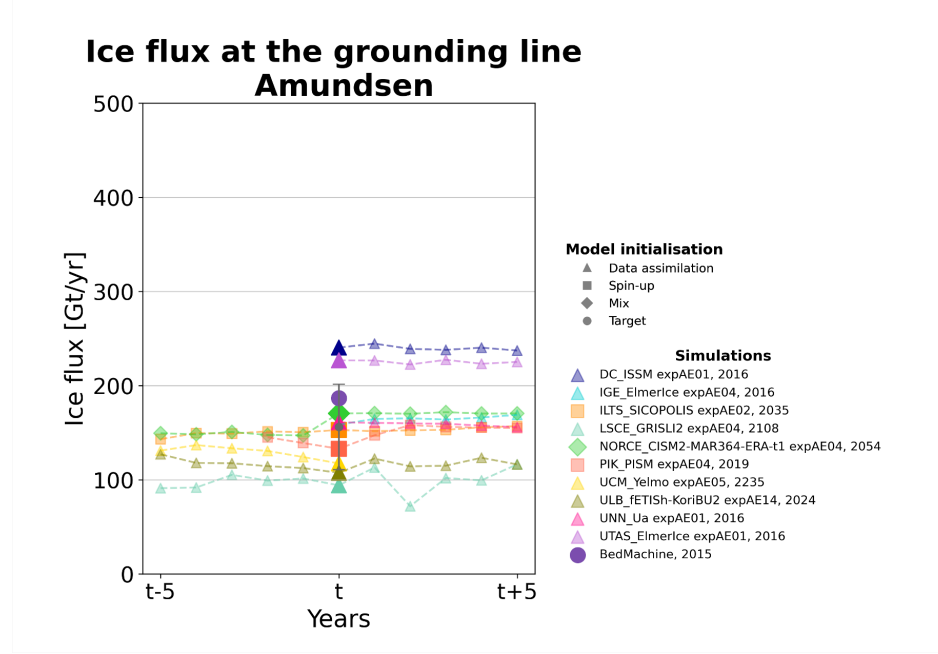


Figure 13: Plot of the ice flux at the grounding line in  $\text{Gt.yr}^{-1}$  for the best year match in relative time. The color indicates the model and the shape of the marker shapes indicate the type of initialization: triangle for DA, square for SP, and diamond for mix initialization DA plus SP. The violet round marker represents the target. The gray point represent the mean of the IF at the GL and the error bar the standard deviation on the ensemble

Based on the BedMachine geometry and velocity observations [Rignot et al. [2017]], we compute a observed IF at the GL of  $190 \text{ Gt.yr}^{-1}$  while model IF at the GL vary from  $95 \text{ Gt.yr}^{-1}$  to  $250 \text{ Gt.yr}^{-1}$ . The closest IF from the target is NORCE CISM2-MAR364-ERA-t1 (in 2054) with an IF at the GL of  $180 \text{ Gt.yr}^{-1}$ , while the best match geometry, IGE Elmer/Ice (in 2016), exhibits a  $155 \text{ Gt.yr}^{-1}$ . Overall, the spread in IF values at  $t$  is significant. Even among DA models, which share a similar initial geometry and timing, the IF values are widely scattered. Conversely, SP models yield values closer to the target, with a narrower spread, albeit generally below the target IF.

#### 4.1.2 Comparison with LSCE GRISLI2

For the limited GL retreat target, we use LSCE GRISLI2, experiment 4 in 2149, a SP model.

Table 5: Summary of model experiments and corresponding year with the lowest RMSE compared to LSCE GRISLI2 target in 2149 (sorted by increasing RMSE)

Simulation	Experiment	Year	RMSE	Initialization
LSCE_GRISLI2	expAE04	2149	0.000000	SP with geometry target
DC_ISSM	expAE10	2026	0.014818	DA
ILTS_SICOPOLIS	expAE14	2089	0.015669	Paleo SP
UCM_Yelmo	expAE03	2189	0.018735	DA
NORCE_CISM2-MAR364-ERA-t1	expAE04	2070	0.019224	DA and SP
IGE_ElmerIce	expAE01	2029	0.019292	DA
UTAS_ElmerIce	expAE05	2033	0.019359	DA
UNN_Ua	expAE15	2020	0.019437	DA ans inversion
PIK_PISM	expAE01	2020	0.019481	SP
ULB_fETISH-KoriBU2	expAE01	2021	0.023310	DA

Using RMSE, the closest match is DC ISSM, experiment 10 in 2026 Tab. 5. Fig 14 presents the associated diagnostics (see Fig. 26, p. 34 for the other match).

While surface elevation fields are comparable, DC ISSM exhibits a more detailed velocity pattern. This could be attributed to its high native resolution (up to 2 km) as well as the 8 km resolution used for the ISMIP outputs, compared to 16 km for LSCE GRISLI2 native (and output) resolution. Indeed, despite our regridding to a 4 km resolution for all models, their initial resolution still affects the outputs. Furthermore, both models show similar velocity magnitudes, but DC ISSM displays broader regions of high velocity.

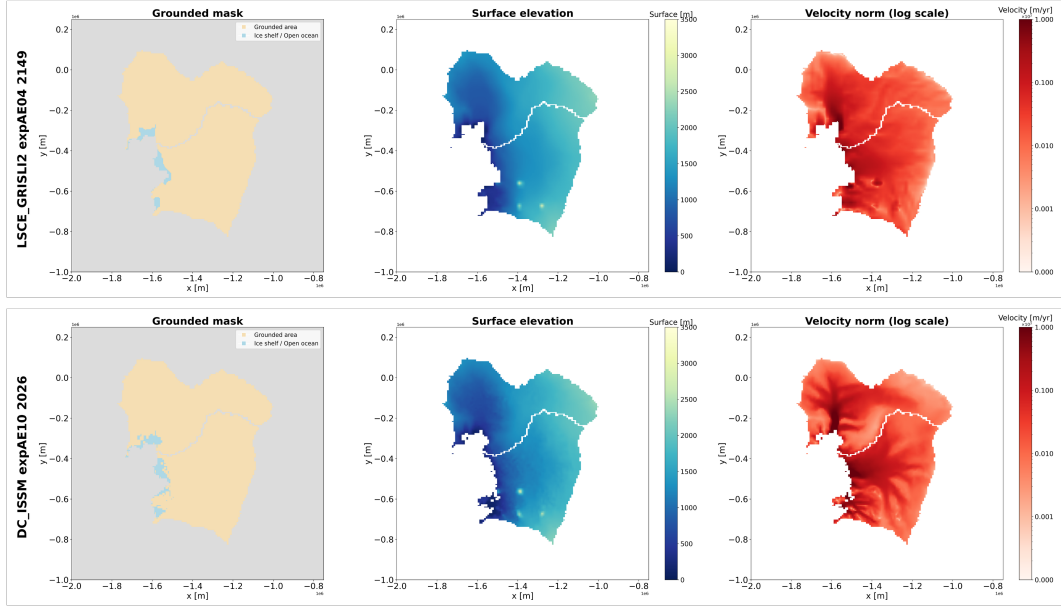


Figure 14: Plot of the diagnostic, for (first line) the target LSCE GRISLI2 experiment 4 in 2149, and (second line) for DC ISSM experiment 10 in 2026. From left to right: the grounding mask, surface elevation in m, and the velocity in  $\text{m.yr}^{-1}$ .

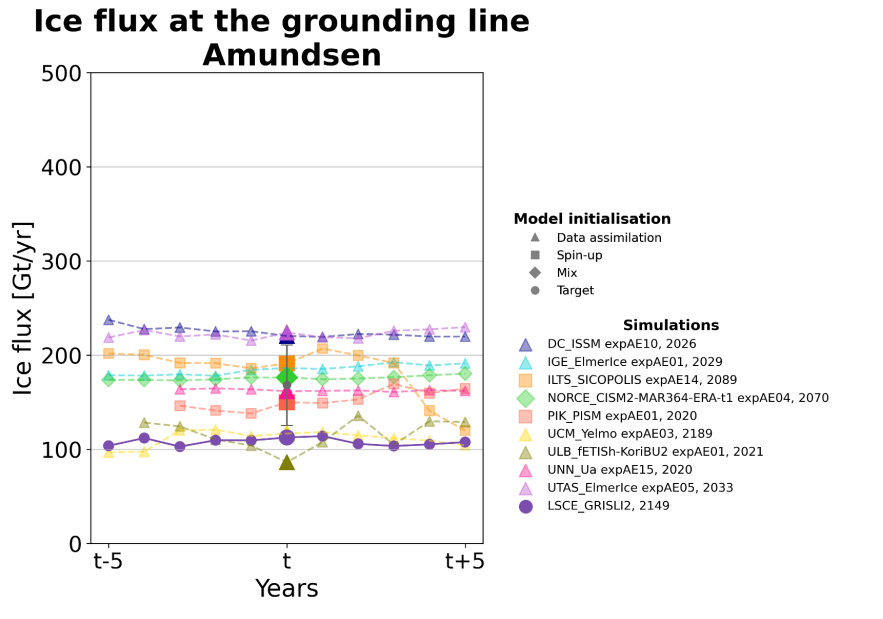


Figure 15: Plot of the ice flux at the grounding line in  $\text{Gt.yr}^{-1}$  for the best year match in relative time. The color of the scatter and the plot represent the model and the shape of the scatter the type of initialization; triangle for DA, square for SP, and diamond for mix initialization DA plus SP. The violet round scatter represent the target. The gray scatter represent the mean of the IF at the GL and the error bar the standard deviation

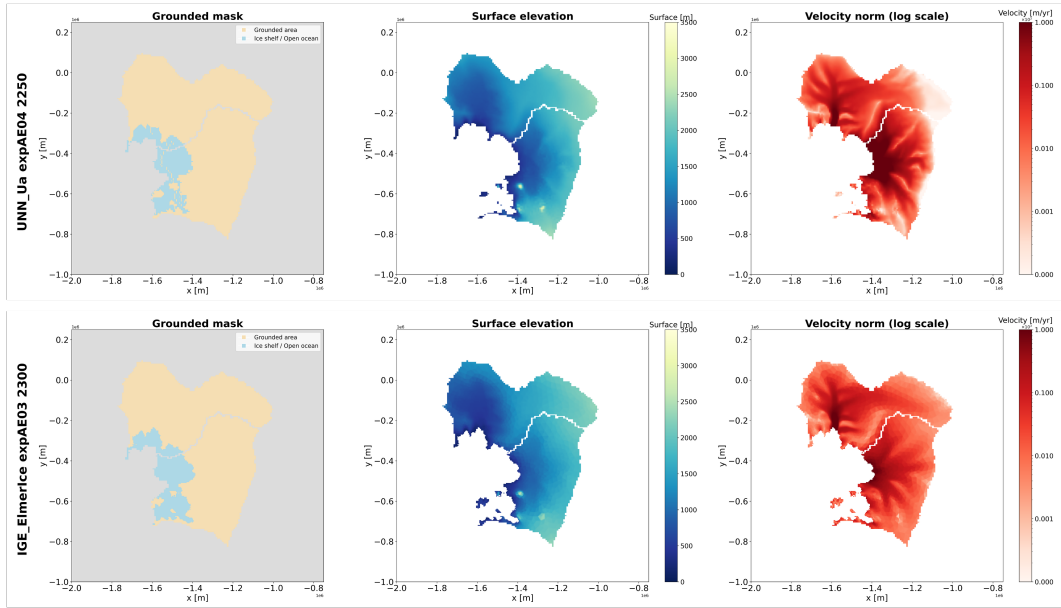
Similarly to the BedMachine comparisons, the IF spread for this limited GL retreated target is large, from  $90 \text{ Gt.yr}^{-1}$  (ULB fETISH-KoriBU2) to  $220 \text{ Gt.yr}^{-1}$  (UTAS Elmer/Ice). The ensemble presents a IF of  $180 \text{ Gt.yr}^{-1}$  in average with a standard deviation of  $45 \text{ Gt.yr}^{-1}$ . The best match in terms of geometry target is DC ISSM have an IF of  $215 \text{ Gt.yr}^{-1}$  in comparison to the  $105 \text{ Gt.yr}^{-1}$  of the target (LSCE GRISLI2). UCM Yelmo , which does not have a good geometry match, almost aligns with the target IF with a value of  $110 \text{ Gt.yr}^{-1}$ , very close to the  $105 \text{ Gt.yr}^{-1}$  of the target (LSCE GRISLI2). DA models show the widest spread (from  $90$  to  $220 \text{ Gt.yr}^{-1}$ ), though two of them closely match the target. Their target years are also close to the present day and close to BedMachine comparison one. SP models exhibit more consistency, but no distinct clusters between SP and DA models emerge in this case. Additionally, the spread remains stable across the  $\pm 5$  year range.

#### 4.1.3 Comparison with UNN Ua

In this section, we use UNN Ua in 2250 as the target model for the large GL retreat scenario. The best grounded mask match is IGE Elmer/Ice experiment 3 in 2300 (Tab. 6). The corresponding diagnostics are shown in Fig. 16 while the diagnostics for the other matches are provided in Fig. 27, p. 35.

Table 6: Summary of model experiments compared to UNN Ua mask in 2250 (sorted by increasing RMSE)

Simulation	Experiment	Year	RMSE	Initialization
UNN_Ua	expAE04	2250	0.000000	DA and inversion
IGE_ElmerIce	expAE03	2300	0.016371	DA
DC_ISSM	expAE03	2300	0.016672	DA
ULB_fETISH-KoriBU2	expAE05	2138	0.018769	DA
PIK_PISM	expAE03	2289	0.020061	SP
ILTS_SICOPOLIS	expAE04	2236	0.023805	Paleo SP
LSCE_GRISLI2	expAE13	2262	0.024166	SP with geometry target
UCM_Yelmo	expAE12	2300	0.026593	DA
UTAS_ElmerIce	expAE03	2254	0.027275	DA
NORCE_CISM2-MAR364-ERA-t1	expAE04	2213	0.029746	DA and SP

Figure 16: Plot of the diagnostic, for (first line) the target UNN Ua experiment in 2250, and (second line) for IGE Elmer/Ice experiment 3 in 2300. From left to right: the grounding mask, surface elevation in m, and the velocity in  $\text{m.yr}^{-1}$ .

In both cases, the grounding line is largely retreated with respect to present day conditions. However, major differences are observed in the Thwaites and Pine Island Glacier regions (see Fig. 24, p. 32), where the target model (UNN Ua) exhibits a larger retreat than IGE Elmer/Ice.

The target (UN Ua) and the best match (IGE Elmer/Ice) have similar spatial repartition of surface elevation, with the same regions characterized by high and low topography. But they differ in magnitude by up to approximately 200 m. The same pattern is observed for the velocities, where the spatial repartition is similar but the ice flow speeds along the valleys and embayments are higher for the target than for IGE Elmer/Ice. While both models use a very similar approach for initialization and share the same underlying physics (both using the SSA), a plausible explanation for the observed differences in ice flow speed could lie

in the choice of basal friction law. Unfortunately, while we know that the IGE Elmer/Ice model employed a linear Weertman friction law, Seroussi et al. [2024] unfortunately does not provide details about the friction law used in the UN Ua model. However, the higher velocities obtained by the latter could be attributed to the use of a non-linear friction law.

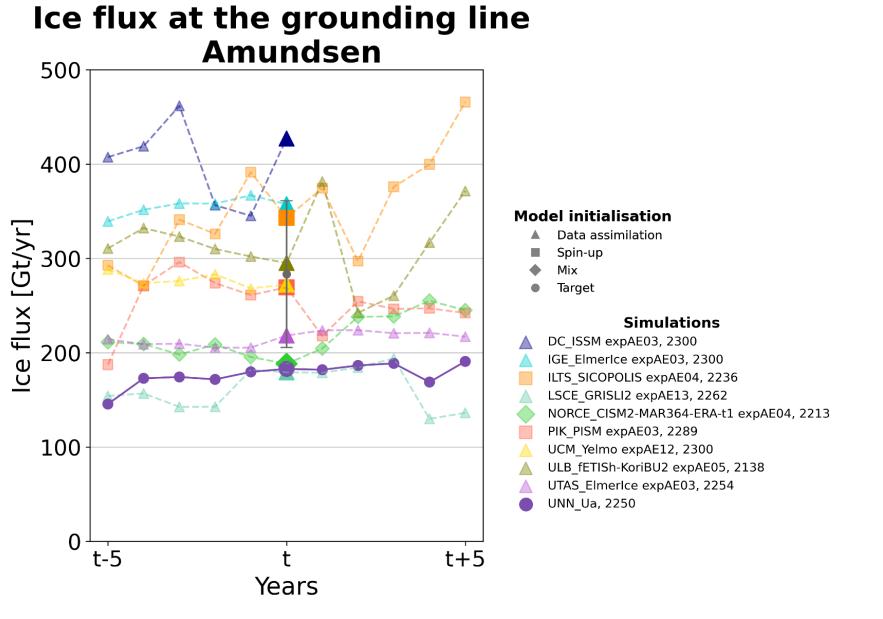


Figure 17: Plot of the ice flux at the grounding line in  $\text{Gt.yr}^{-1}$  for the best year match in relative time. The color of the scatter and the plot represent the model and the shape of the scatter the type of initialization; triangle for DA, square for SP, and diamond for mix initialization DA plus SP. The violet round scatter represent the target. The gray scatter represent the mean of the IF at the GL and the error bar the standard deviation

The IF at the GL with a large GL retreat is represented in Fig. 17.

The IF spread is significant going from  $190 \text{ Gt.yr}^{-1}$  to  $420 \text{ Gt.yr}^{-1}$  with a mean of  $290 \pm 85 \text{ Gt.yr}^{-1}$ , a roughly 60% increase in IF with respect to the more advanced GL target discussed previously. The model spread is primarily due to the spread among SP models, from  $190 \text{ Gt.yr}^{-1}$  to  $420 \text{ Gt.yr}^{-1}$ , while DA models range from  $195 \text{ Gt.yr}^{-1}$  to  $350 \text{ Gt.yr}^{-1}$ .

The best match in terms of grounded mask geometry (i.e. RMSE), IGE ElmerIce, shows a  $260 \text{ Gt.yr}^{-1}$ , the second highest value after DC ISSM. This good match between the two models supports the relationship between grounded mask geometry and grounding line IF.

The target IF is around  $195 \text{ Gt.yr}^{-1}$  and the closest mode (in terms of IF) are NORCE CISM2 (DA and SP) and LSCE GRISLI2 (SP). While the first model has surprisingly the worst match in terms of RMSE, the latter exhibits a RMSE on par with most other models. Most models also show a higher inter-annual variability than in the previous comparisons.

It is also important to notice that UNN Ua IF at the GL is small when its velocities are larger than other in other models. This could be due to the differences in ice thickness closely upstream the grounding line or thicker ice shelves providing more buttressing.

## 4.2 Discussion

Our results show that, overall, the IF at the GL increases with the retreat of the GL. Specifically, the mean IF at the GL for the limited GL retreat scenario is  $160 \text{ Gt.yr}^{-1}$  and  $165 \text{ Gt.yr}^{-1}$  for BedMachine whereas for the large GL retreat it reaches  $290 \text{ Gt.yr}^{-1}$ . This is consistent with expectations: as the grounding line retreats, the ice thickness at the GL increases, which leads to an increased flux based, in agreement with the BL layer theory (see Eq. 8) (some models use Eq. 8 as a boundary condition for IF at the GL). Even though the confirmation may seem obvious in a two-dimensional flow line model, in this case, the ice shelves exert a buttressing effect on the upstream ice flow. In certain configurations, the buttressing effect can stabilize the GL retreat, even on a retrograde bed slope [Gudmundsson et al. [2012]]. It is also important to remind that this analysis is independent of climate forcing, which supports the conclusion that the internal dynamics of the ice sheet is likely the primary factor controlling the velocity of outlet glaciers.

Additionally, we observe that the spread in IF is larger for the large GL retreat scenario compared to the limited ones. The inter-annual variability follows a similar trend. This can likely be attributed to a more dynamic GL position, which in turn impacts the IF. For example, in the large retreat scenario, the IF at the GL for ULB fETISh-KoriBU2 fluctuates from  $390 \text{ Gt.yr}^{-1}$  to  $250 \text{ Gt.yr}^{-1}$  in one year. If we look at ULB fETISh-KoriBU2 grounded masks corresponding to those years (Fig. 28, p. 36), we can see that the grounded mask is more retreated (a few pixels) in 2139 than in 2140 in Thwaites and Crosson regions (see Fig. 24, p. 32). Considering that these few pixels correspond to a 16 km shift in the actual grounding line position, it represents a large variation for the actual GL position.

Our first intuition was that the initialization method of the models had an impact on the IF at the GL. Therefore, the clusters (i.e. the difference we made between DA and SP models) discussed previously were based on this assumption. For example, DA models usually reproduce the current state of the ice sheet better than SP models. This reflects in the ability of the DA models to simulate IF values that are closer to observations, and a time that aligns more closely with the timing of observations. However, this ability to mimic present-day conditions does not necessarily guarantee better projections of the future evolution of the ice sheet, particularly over multi-century timescales. As a matter of fact, the initialization plays a weaker influence on the model after 75 years of run [Seroussi et al. [2024]]. Accounting for this statement, we can look at other model specifications that separate the models into different clusters.

For instance, looking at the figure of IF at the GL in the case of a relatively close to present-day conditions (i.e., the LSCE GRISLI2 target), we could define three different clusters of models:

- DC ISSM, UTAS Elmer/Ice, IGE Elmer/Ice and Ua show relatively high and similar values of IF. All these four models rely on a DA method that optimize both the basal friction and ice fluidity based on current day observations. This optimization of the fluidity usually allows to take account for the apparent lower fluidity in the shear margins, accelerating the ice flow with respect to models only accounting for ice temperature. This fixed fluidity also reduce the degree of freedom of the models for diverging from one another. All these models also present a very similar timing for their best match.
- ILTS SICOPOLIS, PIK PISM and NORCE CISM2 exhibit IF comparable to the first cluster, despite not relying on similar optimization techniques. However, two of these models reach such high ice fluxes much later in the simulation. This delayed increase may result from reduced buttressing due to progressive ice shelf thinning over time. Additionally, the use of a sliding law based on subglacial hydrology and effective pressure (likely to enhancing sliding over time) in these models could explain the IF at the GL and flow velocities they reach, even in the absence of enhanced shear margin fluidity.
- LSCE GRISLI2, UCM Yelmo, and ULB fETISh-KoriBU2 detach from the other models with significantly lower IF at the GL, around  $100 \text{ Gt.yr}^{-1}$ . These models could suffer from their relatively low

resolution in regions such as the Amundsen where narrow and deep ice streams are smoothed out.

This tentative clustering based on relatively limited GL retreat partially translates to geometries with a more advanced grounding line retreat. For example, DC ISSM and IGE Elmer/Ice both display relatively high fluxes for this configuration. However, UNN Ua delivers relatively low ice flux, as discussed previously. On the other side of the IF range, LSCE GRISLI2 keeps showing low IF with respect to the other models but UCM Yelmo and ULB fETISH-KoriBU2 seem to have raised to IF values closer to the other model clusters.

Although our primary goal was to disregard the time-dependence of the model states (i.e. the grounding line usually retreats over time), we have observed that the year of the best match for the DA models is close to present days and, therefore the reference time for BedMachine, except for UCM Yelmo. Looking at the evolution of the relative distance of the GL distance over the years (cf. Fig. 11, p. 17), UCM Yelmo GL exhibits a very small retreat, with a GL that remains several kilometers to several tens of kilometers upstream of the present day GL, even beyond 2100. This could explain the differences in years to the other DA models. The fact that the matching years for the limited GL retreat scenario closely coincide with BedMachine's reference suggests that LSCE GRISLI2 GL retreat is too close to the actual one. Choosing a target GL position more retreated than the present-day one might have been more appropriate and should be considered in the following of this work.

For the UNN Ua comparison, it is the opposite, the matching years for all models are close to 2300 (the end of the run). However, most matches exhibit a higher RMSE than in the two other comparison cases (i.e. with BedMachine and LSCE GRISLI2). This suggests that either the models diverge more significantly when the grounding line retreats far inland (likely due to increased differences as the simulation progresses) or that better matches might have occurred after 2300 if the simulations had been extended further. Either way, the greater geometric mismatch (i.e. the larger variations in GL position) between the target and the comparison models may explain the differences in IF at the GL (see Fig. 27, p. 35).

We can also assess the impact of the differences in GL geometry (using RMSE) on the difference between the target and comparison model IF. Here, the relative flux,  $\Delta F$ , is defined as:

$$\Delta F = |F_{\text{comparison}} - F_{\text{target}}|$$

The following Figure (see Fig.18, p. 27) represents the RMSE over the relative flux for each model match for the three targets.

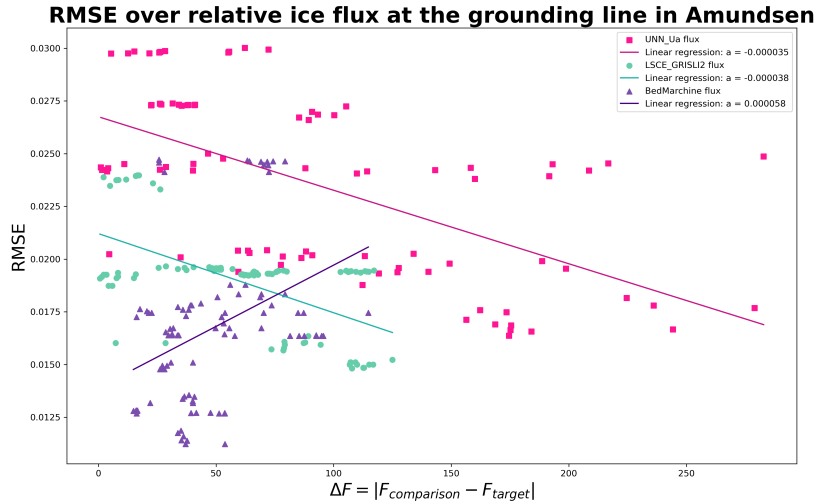


Figure 18: RMSE of the  $\Delta F$  at the grounding line for the matches to Amundsen targets in the  $\pm 5$  years. The color and shape of each scatter point indicate the corresponding target. Linear regressions are shown in matching colors, along with the slope values indicating the trend precision ( $a$ ).

For the difference in GL geometry to significantly influence the difference of the IF at the GL respective to the target value, the slope of the linear regression would need to be positive. If our hypothesis is valid (that the flux is primarily controlled by the geometry), we would expect a positive relationship; specifically, the difference in flux relative to the target should increase as the RMSE grows.

However, as shown in Fig. 18, two of the slopes ( $a$  in the legend) are negative (UNN Ua and LSCE GRISLI2) and one is positive (BedMachine). Therefore, we find a positive correlation between the differences in geometry and the spread in IF for BedMachine comparison. This correlation can be explained by the fact that the DA models have a similar initialization as BedMachine. For the other target, it indicates that the RMSE does not account for most of the flux differences between models and their targets. While this might highlights the limitation of the RMSE on the grounded mask geometry (or any other scalar scoring) when it comes to accurately quantify the difference between complex 3D geometries, it remains important to look the RMSE evaluation to all models and experiments across the entire simulation period. Here, we have focused on a  $\pm 5$  year window around our model best match. However, given the consistency of a model IF and geometry over a short period of time (i.e. models evolve slowly), this limited time window might not be sufficient to fully assess the relevance and limitations of our RMSE metric. Extending this evaluation across the entire simulation period should be a key objective in future work.

In the end, this plot reinforce the key result that the larger the retreat of the grounding line, the greater the spread and variability in the associated ice flux. This contrasts with the more constrained fluxes observed for the limited GL retreat scenario and the present-day geometry. While this highlights the growing uncertainty under larger GL retreat, it also underscores the importance of improving the understanding of models at representing ice dynamics at the grounding line.

## 5 Conclusion and Perspective

To conclude, assessing the contribution of the Antarctic ice sheet requires quantifying the ice flux at the grounding line, which feeds the ice shelves. Based on Eq. 8, and under the assumptions that this equation can be applied to three-dimensional models, that models sharing the same sliding law and rheology should behave similarly, and that ice thickness at the GL should be comparable if the grounding line position is the same. We aimed to evaluate whether models with similar GL geometries produce similar ice fluxes at the grounding line. To do so, we used the RMSE as a metric to identify comparable GL geometries between models in the ISMIP6 ensemble. Our analysis was conducted using three different targets: the observed geometry from BedMachine, a scenario with limited grounding line retreat, and a scenario with a large grounding line retreat. We focused on the Amundsen Sea sector, as this region represents a key potential contributor to future sea-level rise.

First, it clearly shows that flux increases with the retreat of the grounding line. This behavior is consistent across all models and targets, and aligns with theoretical expectations.

However, the increase of the ice flux at the grounding line is accompanied by a greater spread and the annual variability for the  $\pm 5$  years. For all targets, the spread is very large. This is particularly problematic for the observed geometry, as it suggests that some models still struggle to accurately represent present-day fluxes.

When comparing to the actual geometry, DA models show the best agreement in both geometry and ice flux at the grounding line. This result is reassuring, considering that DA models are designed to match observations. However, the IF at the GL for the DA models are not exactly accurate to the observed one. This raise further question regarding the impact of the sliding in those models, and with what accuracy they reproduce the IF at the GL. It would be worth investigating whether we can find cluster based on the sliding law used inside the DA model ensemble.

Moreover, the use of RMSE as a matching criterion appears to have its limitations. Even when the RMSE is minimized, the geometry of the grounded masks can remain significantly different, and small pixel mismatches may correspond to large real-world differences of the grounding line (up to 16 km for some models). Another step would be to explore model emulator,statistical model that would predict the IF at the GL for a model at a chosen grounding line, to improve the consistency between model geometries and better assess the impact of this latter on the IF at the GL.

Additionally, it may be interesting to investigate other factors to explain the differences in ice flux at the grounding line. For instance, models use different initial grid structures: some refine the resolution near the grounding line, while others keep a consistent resolution across all the domain. Could this affect their ability to resolve fluxes at the GL?

Finally, it is important to note that this analysis has so far been limited to a single region. To further assess these findings, similar comparisons should be conducted in other key sectors of the Antarctic ice sheet, such as the Ross Sea sector, where retreat–combined with that of the Amundsen sector–could lead to the total collapse of the West Antarctic Ice Sheet. The geological differences between the regions, i.e. a smoother and less complex bedrock topography, could also affect our results in a different way. Comparing the performance of different models and sliding laws in this region could help identify whether some parameterizations are

more specific to certain regions, and whether certain models exhibit more similar geometries and ice fluxes.

# Appendix

Table 7: List of acronyms used in the report

Acronym	Name
AIS	Antarctic ice sheet
AMB	Antarctic mass balance
GHG	Greenhouse gases
GL	Grounding line
HD	Hausdorff distance
IF	Ice flux
MICI	Marine ice cliff instability
MISI	Marine ice sheet instability
SIA	Shallow ice approximation
SLR	Sea-level rise
SSA	Shallow shelf approximation
SSH	Sea surface height

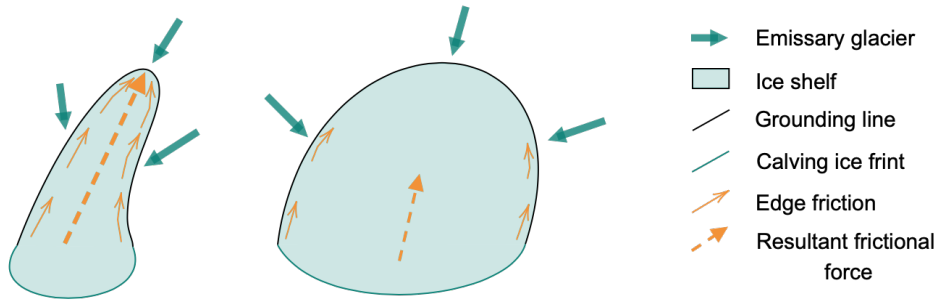


Figure 19: Schematic diagram of the effect of bay geometry friction on the velocity of ice flux. On the left narrow glacier embayment and on the right wider glacier embayment.

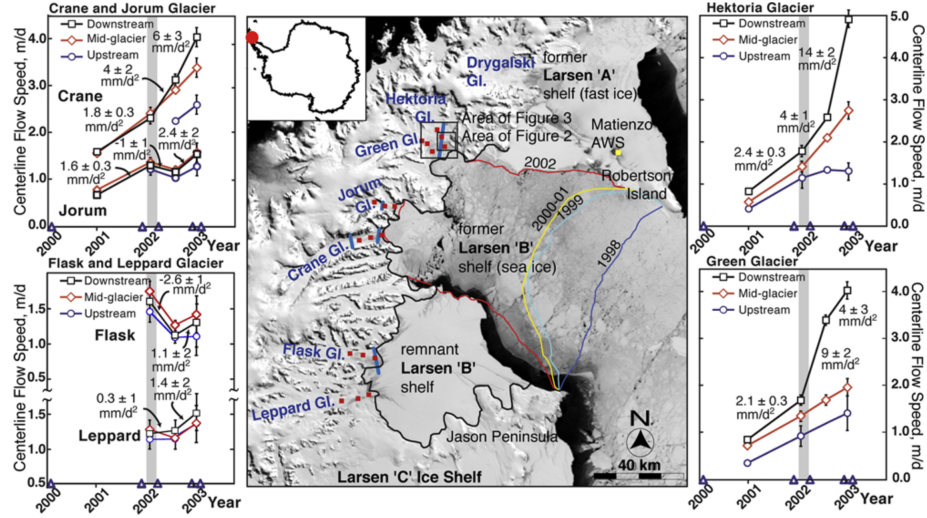


Figure 20: Figure from Scambos et al. [2004], representing the effect of the presence of an ice shelf on ice flow velocity. Center panel: satellite image from November 1st, 2003 of Antarctica peninsula, lines are calving ice front of the ice shelf at the given time. Surrounding graphs: ice speed and downstream site acceleration for the six glacier before during and after the collapse of the ice shelf (computed using satellite images).

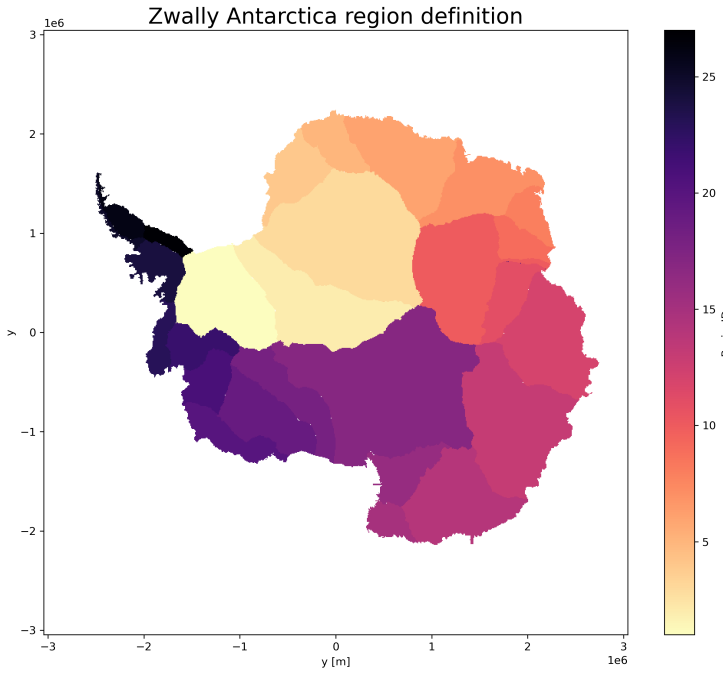


Figure 21: Plot of Zwally Antarctica region definition, Basin.ID correspond to the number of each drainage basin. Amundsen region correspond to basin number 21 and 22, and Ross region to 18 and 19.

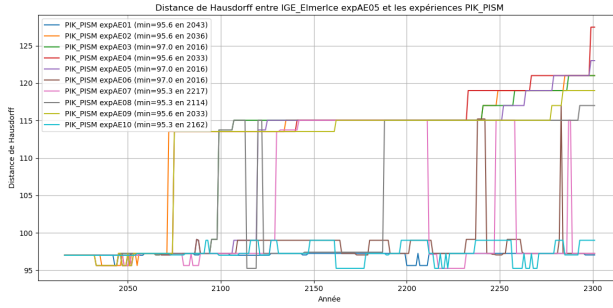


Figure 22: Plot of the Hausdorff distance over time between IGE Elmer/Ice, as a target, and PIK PISM experiment.

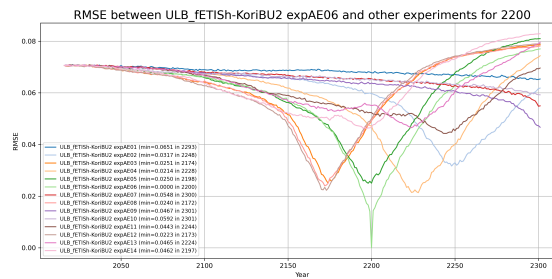


Figure 23: RMSE over time within experiments of a model.

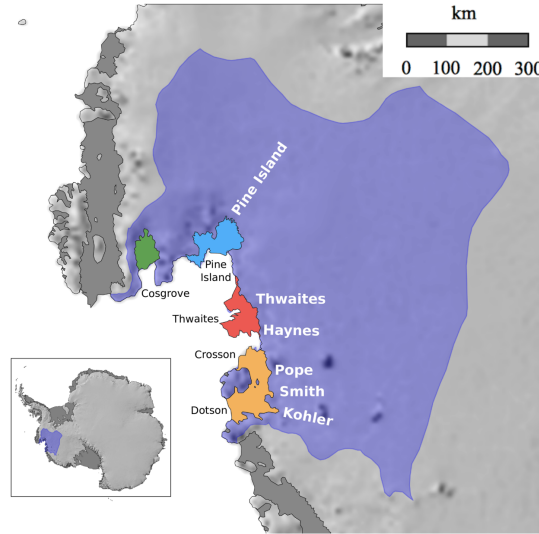


Figure 24: Definition of the region and glacier in Amundsen Sea Sector from [Brondex et al. [2019]]

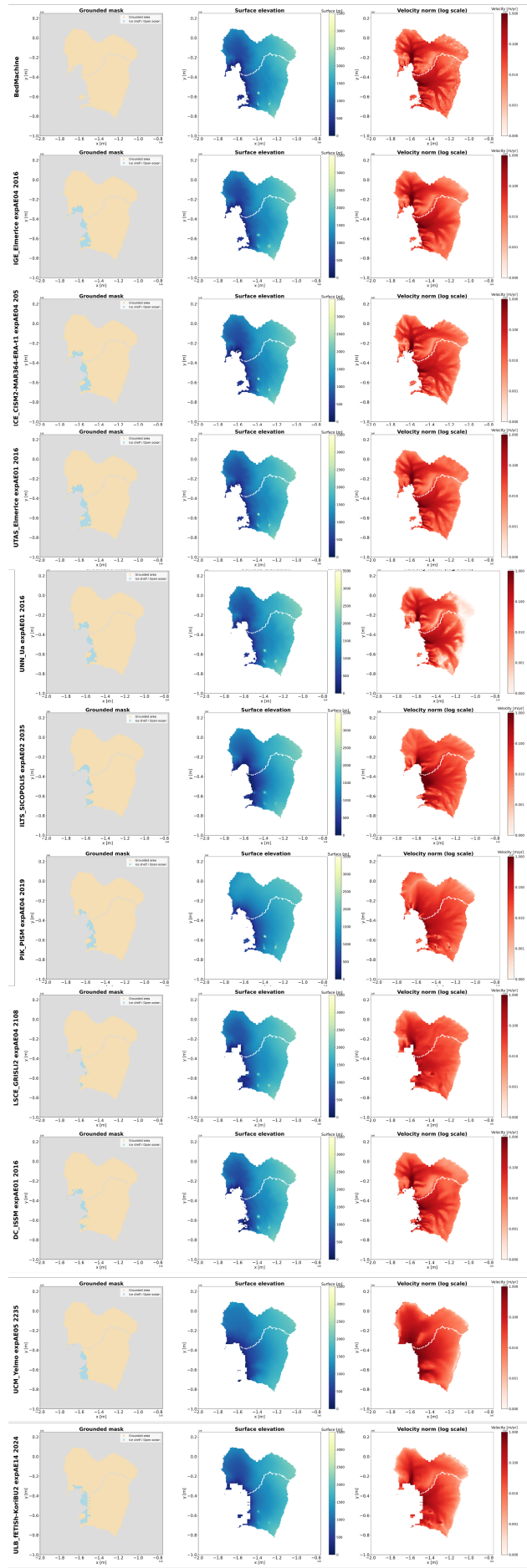


Figure 25: All matches diagnostics for BedMachine target

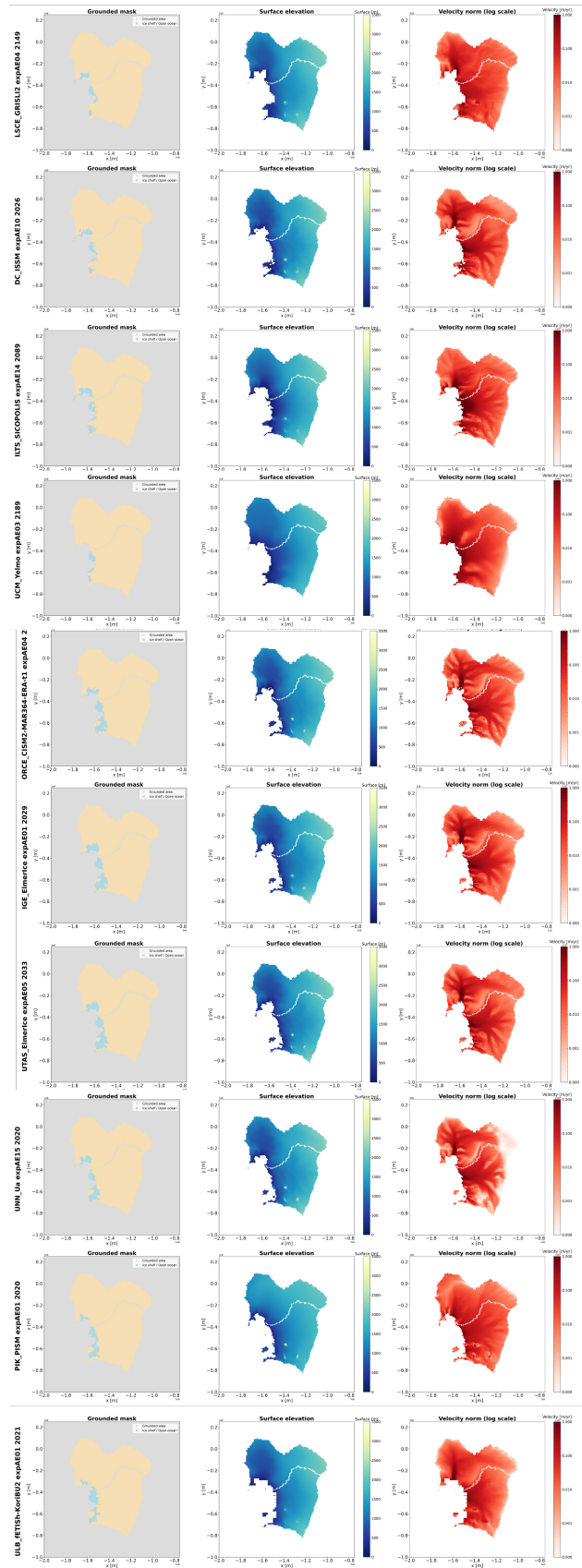


Figure 26: All matches diagnostics for LSCE GRISLI2 target

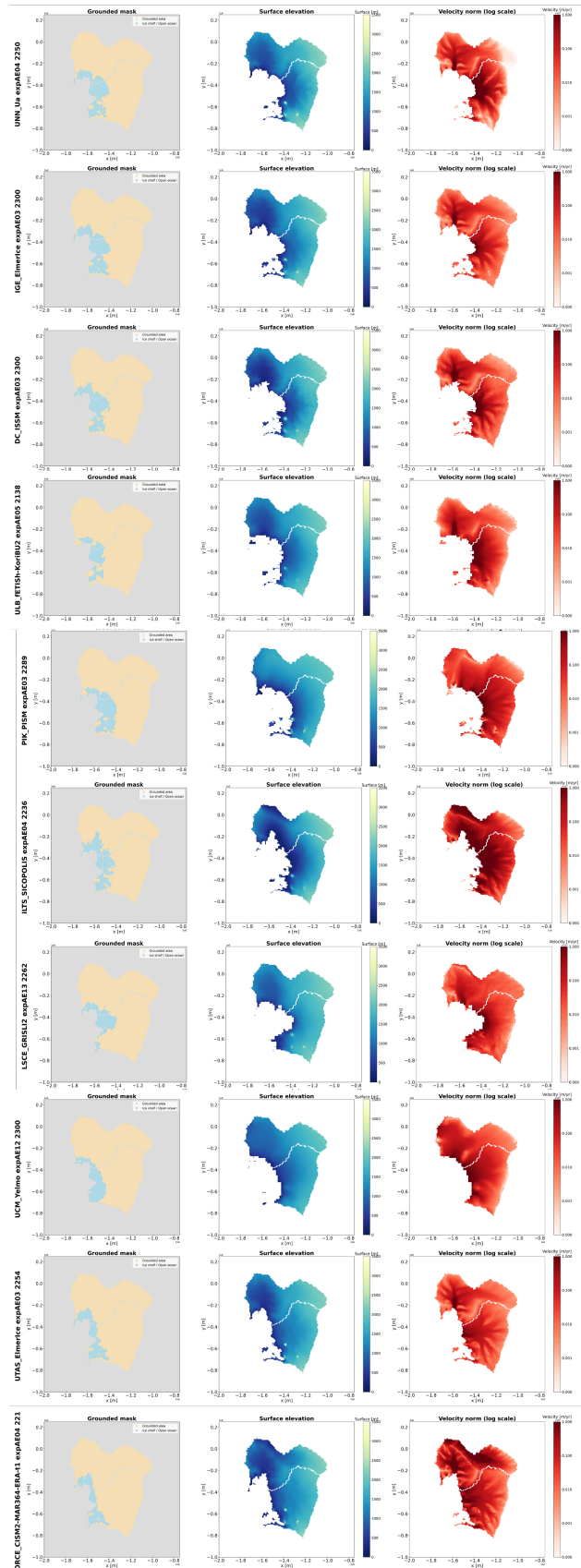
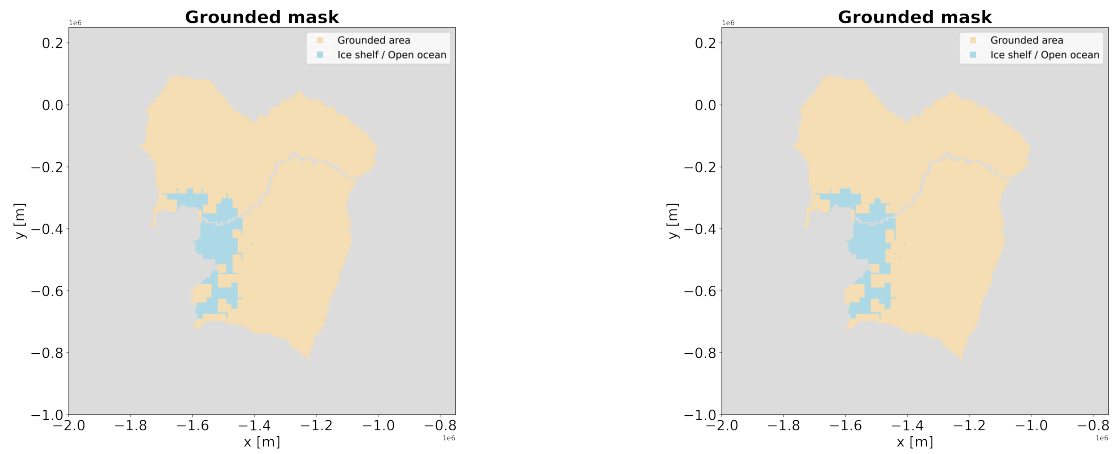


Figure 27: All matches diagnostics for UNN\_Ua target



(a) ULB fETIsh-KoriBU2 grounded at  $t + 1$  (2139)  
after the match with UNN Ua

(b) ULB fETIsh-KoriBU2 grounded at  $t + 2$  (2140)  
after the match with UNN Ua

Figure 28: ULB fETIsh-KoriBU2 grounded masks in AMUN region

# References

- J. Brondex, O. Gagliardini, F. Gillet-Chaulet, and G. Durand. Sensitivity of grounding line dynamics to the choice of the friction law. *Journal of Glaciology*, 63:854–866, 2017.
- J. Brondex, F. Gillet-Chaulet, and O. Gagliardini. Sensitivity of centennial mass loss projections of the amundsen basin to the friction law. *The Cryosphere*, 13:177–195, 2019. doi: 10.5194/tc-13-177-2019.
- K. Calvin, D. Dasgupta, G. Krinner, A. Mukherji, P. W. Thorne, C. Trisos, J. Romero, et al. *Climate Change 2023: Synthesis Report. Contribution of Working Groups I, II and III to the Sixth Assessment Report of the Intergovernmental Panel on Climate Change*. Intergovernmental Panel on Climate Change (IPCC), Geneva, Switzerland, first edition, 2023. doi: 10.59327/IPCC/AR6-9789291691647. URL <https://doi.org/10.59327/IPCC/AR6-9789291691647>. Core Writing Team, H. Lee and J. Romero (Eds.).
- A. Cazenave. How fast are the ice sheets melting? *Science*, 314(5803):1250–1252, 2006. doi: 10.1126/science.1133325.
- Cryospheric Sciences. Image of the week – kicking the ice’s butt(ressing), May 2019. URL <https://blogs.egu.eu/divisions/cr/2019/05/10/image-of-the-week-kicking-the-ices-buttrressing/>.
- R. M. DeConto and D. Pollard. Contribution of antarctica to past and future sea-level rise. *Nature*, 531(7596):591–597, 2016. doi: 10.1038/nature17145. URL <https://doi.org/10.1038/nature17145>.
- T. L. Edwards. Revisiting antarctic ice loss due to marine ice-cliff instability. *Nature*, 566, 2019.
- J. Feldmann and A. Levermann. Collapse of the west antarctic ice sheet after local destabilization of the amundsen basin. *Proceedings of the National Academy of Sciences*, 112(46):14191–14196, 2015. doi: 10.1073/pnas.1512482112.
- J. W. Glen. The creep of polycrystalline ice. *Proceedings of the Royal Society of London. Series A, Mathematical and Physical Sciences*, 228(1175):519–538, 1955. doi: 10.1098/rspa.1955.0066. URL <https://doi.org/10.1098/rspa.1955.0066>.
- G. H. Gudmundsson, J. Krug, G. Durand, L. Favier, and O. Gagliardini. The stability of grounding lines on retrograde slopes. *The Cryosphere*, 6(6):1497–1505, 2012. doi: 10.5194/tc-6-1497-2012. URL <https://doi.org/10.5194/tc-6-1497-2012>.
- S. Hallegatte. A framework to investigate the economic growth impact of sea level rise. *Environmental Research Letters*, 7(1):015604, Jan. 2012. doi: 10.1088/1748-9326/7/1/015604. URL <https://doi.org/10.1088/1748-9326/7/1/015604>.
- J. Hansen, M. Sato, G. Russell, and P. Kharecha. Climate sensitivity, sea level and atmospheric carbon dioxide. *Philosophical Transactions of the Royal Society A: Mathematical, Physical and Engineering Sciences*, 371(2001):20120294, 2013. doi: 10.1098/rsta.2012.0294. URL <https://doi.org/10.1098/rsta.2012.0294>.
- E. A. Hill, B. Urruty, R. Reese, J. Garbe, O. Gagliardini, G. Durand, F. Gillet-Chaulet, S. L. Cornford, G. R. Leguy, X. Asay-Davis, T. L. Edwards, T. Zwinger, F. Pattyn, H. Seroussi, R. S. Smith, H. Gudmundsson, S. Nowicki, M. Zeitz, and A. Levermann. The stability of present-day antarctic grounding lines – part 1: No indication of marine ice sheet instability in the current geometry. *The Cryosphere*, 17(9):3739–3759, 2023. doi: 10.5194/tc-17-3739-2023.

- IPCC. Summary for policymakers — special report on the ocean and cryosphere in a changing climate, 2019. URL <https://www.ipcc.ch/srocc/chapter/summary-for-policymakers/>. Accessed: 2025-05-07.
- I. Joughin, B. E. Smith, and C. G. Schoof. Regularized coulomb friction laws for ice sheet sliding: Application to pine island glacier, antarctica. *Geophysical Research Letters*, 46(9):4764–4771, May 2019. doi: 10.1029/2019GL082526. URL <https://doi.org/10.1029/2019GL082526>.
- E. J. Judd, J. E. Tierney, D. J. Lunt, I. P. Montañez, B. T. Huber, S. L. Wing, and P. J. Valdes. A 485-million-year history of earth’s surface temperature. *Science*, 385(6715):eadk3705, 2024. doi: 10.1126/science.adk3705. URL <https://doi.org/10.1126/science.adk3705>.
- E. Larour, H. Seroussi, M. Morlighem, and E. Rignot. Continental scale, high order, high spatial resolution, ice sheet modeling using the ice sheet system model (issm). *Journal of Geophysical Research: Earth Surface*, 117(F1), 2012. doi: 10.1029/2011JF002140.
- NASA. NASA Sea Level Change Portal: Ice Sheets, 2025. URL <https://sealevel.nasa.gov/understanding-sea-level/regional-sea-level/ice-sheets>.
- S. Nowicki, H. Goelzer, H. Seroussi, A. J. Payne, W. H. Lipscomb, A. Abe-Ouchi, C. Agosta, et al. Experimental protocol for sea level projections from ismip6 stand-alone ice sheet models. *The Cryosphere*, 14(7):2331–2368, 2020. doi: 10.5194/tc-14-2331-2020. URL <https://doi.org/10.5194/tc-14-2331-2020>.
- F. Pattyn. Sea-level response to melting of antarctic ice shelves on multi-centennial timescales with the fast elementary thermomechanical ice sheet model (f.etish v1.0). *The Cryosphere*, 11(4):1851–1878, 2017. doi: 10.5194/tc-11-1851-2017.
- F. Pattyn. The paradigm shift in antarctic ice sheet modelling. *Nature Communications*, 9(1):2728, 2018. doi: 10.1038/s41467-018-05003-z. URL <https://doi.org/10.1038/s41467-018-05003-z>.
- A. Quiquet, C. Dumas, C. Ritz, V. Peyaud, and D. M. Roche. The grisl ice sheet model (version 2.0): Calibration and validation for multi-millennial changes of the antarctic ice sheet. *Geoscientific Model Development*, 11(12):5003–5025, 2018. doi: 10.5194/gmd-11-5003-2018.
- E. Rignot, J. Mouginot, M. Morlighem, H. Seroussi, and B. Scheuchl. Widespread, rapid grounding line retreat of pine island, thwaites, smith, and kohler glaciers, west antarctica, from 1992 to 2011. *Geophysical Research Letters*, 41(10):3502–3509, 2014. doi: 10.1002/2014GL060140.
- E. Rignot, J. Mouginot, and B. Scheuchl. Measures insar-based antarctica ice velocity map, version 2. NASA National Snow and Ice Data Center Distributed Active Archive Center, Boulder, Colorado, USA, 2017. URL <https://doi.org/10.5067/D7GK8F5J8M8R>. [data set].
- E. J. Rignot. Fast recession of a west antarctic glacier. *Science*, 281(5376):549–551, 1998. doi: 10.1126/science.281.5376.549.
- A. Robinson, D. Goldberg, and W. H. Lipscomb. A comparison of the stability and performance of depth-integrated ice-dynamics solvers. *The Cryosphere*, 16(2):689–709, 2022. doi: 10.5194/tc-16-689-2022.
- J. Ryu and S. ichiro Kamata. An efficient computational algorithm for hausdorff distance based on points-ruling-out and systematic random sampling. *Pattern Recognition*, 114:107857, June 2021. doi: 10.1016/j.patcog.2021.107857. URL <https://doi.org/10.1016/j.patcog.2021.107857>.
- T. Sato and R. Greve. Sensitivity experiments for the antarctic ice sheet with varied sub-ice-shelf melting rates. *Annals of Glaciology*, 53(60):221–228, 2012. doi: 10.3189/2012AoG60A042.

- T. A. Scambos, J. A. Bohlander, C. A. Shuman, and P. Skvarca. Glacier acceleration and thinning after ice shelf collapse in the larsen b embayment, antarctica. *Geophysical Research Letters*, 31(18), 2004. doi: 10.1029/2004GL020670. URL <https://doi.org/10.1029/2004GL020670>.
- C. Schoof. The effect of cavitation on glacier sliding. *Proceedings of the Royal Society A: Mathematical, Physical and Engineering Sciences*, 461(2055):609–627, 2005. doi: 10.1098/rspa.2004.1350.
- C. Schoof. Marine ice-sheet dynamics. part 1. the case of rapid sliding. *Journal of Fluid Mechanics*, 573: 27–55, 2007a. doi: 10.1017/S0022112006003570.
- C. Schoof. Ice sheet grounding line dynamics: Steady states, stability, and hysteresis. *Journal of Geophysical Research: Earth Surface*, 112(F3), Sept. 2007b. doi: 10.1029/2006JF000664. URL <https://doi.org/10.1029/2006JF000664>.
- H. Seroussi, M. Morlighem, E. Larour, E. Rignot, and A. Khazendar. Hydrostatic grounding line parameterization in ice sheet models. *The Cryosphere*, 8(6):2075–2087, 2014a. doi: 10.5194/tc-8-2075-2014.
- H. Seroussi, M. Morlighem, E. Larour, E. Rignot, and A. Khazendar. Hydrostatic grounding line parameterization in ice sheet models. *The Cryosphere*, 8(6):2075–2087, 2014b. doi: 10.5194/tc-8-2075-2014.
- H. Seroussi, S. Nowicki, E. Simon, A. Abe-Ouchi, T. Albrecht, J. Brondex, S. Cornford, et al. initmip-antarctica: An ice sheet model initialization experiment of ismip6. *The Cryosphere*, 13(5):1441–1471, 2019. doi: 10.5194/tc-13-1441-2019. URL <https://doi.org/10.5194/tc-13-1441-2019>.
- H. Seroussi, T. Pelle, W. H. Lipscomb, A. Abe-Ouchi, T. Albrecht, J. Alvarez-Solas, X. Asay-Davis, et al. Evolution of the antarctic ice sheet over the next three centuries from an ismip6 model ensemble. *Earth's Future*, 12(9):e2024EF004561, Sept. 2024. doi: 10.1029/2024EF004561.
- The IMBIE Team. Mass balance of the greenland ice sheet from 1992 to 2018. *Nature*, 579(7798):233–239, 2020. doi: 10.1038/s41586-019-1855-2.
- V. C. Tsai, A. L. Stewart, and A. F. Thompson. Marine ice-sheet profiles and stability under coulomb basal conditions. *Journal of Glaciology*, 61:205–215, 2015.
- I. Velicogna. Increasing rates of ice mass loss from the greenland and antarctic ice sheets revealed by grace. *Geophysical Research Letters*, 36(19), 2009. doi: 10.1029/2009GL040222.
- J. Weertman. On the sliding of glaciers. *Journal of Glaciology*, 3(21):33–38, 1957. doi: 10.3189/S0022143000024709. URL <https://doi.org/10.3189/S0022143000024709>.
- J. Weertman. Stability of the junction of an ice sheet and an ice shelf. *Journal of Glaciology*, 13(67), 1974.
- M. J. Widlansky, X. Long, and F. Schloesser. Increase in sea level variability with ocean warming associated with the nonlinear thermal expansion of seawater. *Communications Earth & Environment*, 1(1):9, Aug. 2020. doi: 10.1038/s43247-020-0008-8. URL <https://doi.org/10.1038/s43247-020-0008-8>.